NAR Cancer, 2025, **7**, zcaf009
https://doi.org/10.1093/narcan/zcaf009
DNA Damage Sensing and Repair

TRIP13 protects pancreatic cancer cells against intrinsic and therapy-induced DNA replication stress

Jay R. Anand[1], Gaith N. Droby[2], Sayali Joseph[1], Urvi Patel[1], Xingyuan Zhang[1], Jeffrey A. Klomp[3,4], Channing J. Der[3,4], Jeremy E. Purvis[5,6], Samuel C. Wolff[5,6], Jessica L. Bowser[1,3], Cyrus Vaziri[1,2,3,*]

[1]Department of Pathology and Laboratory Medicine, University of North Carolina at Chapel Hill, Chapel Hill, NC 27599, United States
[2]Curriculum in Genetics and Molecular Biology, University of North Carolina at Chapel Hill, Chapel Hill, NC 27599, United States
[3]Lineberger Comprehensive Cancer Center, University of North Carolina at Chapel Hill, Chapel Hill, NC 27599, United States
[4]Department of Pharmacology, University of North Carolina at Chapel Hill, Chapel Hill, NC 27599, United States
[5]Department of Genetics, University of North Carolina at Chapel Hill, Chapel Hill, NC, 27599, United States
[6]Computational Medicine Program, University of North Carolina at Chapel Hill, Chapel Hill, NC, 27599, United States
[*]To whom correspondence should be addressed: Email: cyrus_vaziri@med.unc.edu

Abstract

Oncogene activation in normal untransformed cells induces DNA replication stress and creates a dependency on DNA damage response (DDR) mechanisms for cell survival. Different oncogenic stimuli signal via distinct mechanisms in every cancer setting. The DDR is also pathologically reprogrammed and deployed in diverse ways in different cancers. Because mutant KRAS is the driver oncogene in 90% of pancreatic ductal adenocarcinomas (PDACs), here we have investigated DDR mechanisms by which KRAS-induced DNA replication stress is tolerated in normal human pancreatic epithelial cells [human pancreatic nestin-expressing (HPNE) cells]. Using a candidate screening approach, we identify TRIP13 as a KRAS^{G12V}-induced messenger RNA that is also expressed at high levels in PDAC relative to normal tissues. Using genetic and pharmacological tools, we show that TRIP13 is necessary to sustain ongoing DNA synthesis and viability specifically in KRAS^{G12V}-expressing cells. TRIP13 promotes survival of KRAS^{G12V}-expressing HPNE cells in a homologous recombination (HR)-dependent manner. KRAS^{G12V}-expressing HPNE cells lacking TRIP13 acquire hallmark HR deficiency phenotypes, including sensitivity to inhibitors of translesion synthesis and poly-ADP ribose polymerase. Established PDAC cell lines are also sensitized to intrinsic DNA damage and therapy-induced genotoxicity following TRIP13 depletion. Taken together, our results expose TRIP13 as an attractive new and therapeutically tractable vulnerability of KRAS-mutant PDAC.

Graphical abstract

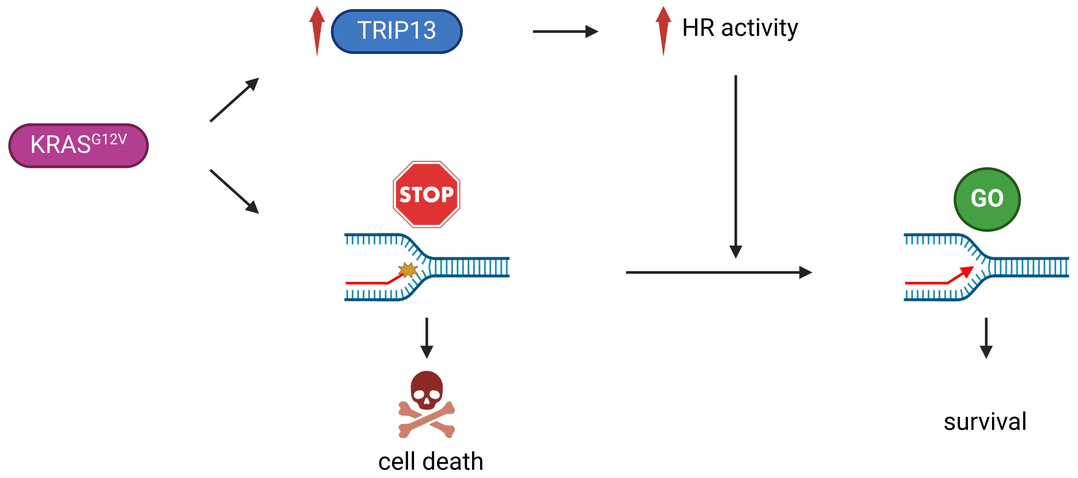

Introduction

For decades, it has been recognized that strong mitogenic stimuli can be cytostatic. For example, excessive growth factor signaling [1–6] or overproduced oncoproteins (including c-MYC [7–13], Cyclin E [11, 14–17], β-catenin [18], and active mutants of KRAS [19–21]) arrest the cell cycle. The cytostatic effects of excessive mitogenic stimulation are often attributed to DNA replication stress and DNA damage. Many mechanisms

Received: July 24, 2024. **Revised:** January 25, 2025. **Editorial Decision:** March 5, 2025. **Accepted:** March 11, 2025

are proposed for why oncogenic stimuli induce replication stress, including refiring of DNA replication origins more than once every S phase, accelerated G1 entry leading to reduced DNA replication licensing, reactive oxygen species, cohesion complex occupancy, R-loops, and transcription replication collisions [22–25]. The DNA damage response (DDR) mechanisms deployed to sense and remediate oncogene-associated DNA replication stress are highly consequential because they dictate cell plasticity and fate, survival, and genome stability.

We and others have previously described some of the DDR mechanisms that respond to oncogenic stimuli [14, 26, 27]. However, past studies have often deployed artificial experimental systems to overexpress oncogenes at levels that are not pathologically relevant. For example, massive overexpression of Cyclin E (at levels up to >10-fold higher than are expressed in cancer cells) is a standard experimental model system [14, 28, 29]. The robust DNA replication stress response elicited by overexpressed Cyclin E is highly atypical of most oncogenic stimuli. Past studies have routinely used Cyclin E to hyperstimulate S phase in cancer cell lines such as U2OS that already experience intrinsic DNA replication stress and have atypical DDR properties when compared with normal cells [11, 14, 15, 17, 26, 28, 30]. Therefore, we have a limited mechanistic understanding of how normal cells respond to pathologically relevant oncogene-associated stresses.

No single mechanism explains responses to DNA replication stresses induced by all oncogenic stimuli. Different oncogenic stimuli act via distinct mechanisms within a given cell type, and the same oncogenic stimulus can frequently elicit different responses in different cell types [31–34]. Similarly, the DDR is reprogrammed and deployed in diverse ways in different cancers [35]. Therefore, it is necessary to determine the relationship between specific oncogenes and the DDR in defined disease-relevant settings. There is no consensus on how oncogenic KRAS induces DNA replication stress or how that stress is remediated. For example, it is reported that KRAS both does [36] and does not [37] induce DNA replication stress. Effects of KRAS signaling are notoriously tissue- and context-specific [32, 38–42] and cellular models for studying responses to KRAS must be chosen carefully to correspond to the disease model.

Oncogenic KRAS drives 90% of pancreatic ductal adenocarcinomas (PDACs) [43, 44]. Of all major cancers, PDAC has the highest mortality rate [45] and the 5-year survival rate of PDAC patients is a dismal 13% [46–48]. Recently developed direct inhibitors of one KRAS mutant, KRAS^{G12C} (G12Ci), have shown promising responses in KRAS^{G12C}-mutant PDAC, supporting the clinical potential of anti-KRAS therapies in PDAC treatment [49, 50]. Although KRAS inhibitors are initially effective for treating PDAC, patients usually relapse as their tumors adapt to KRAS blockade [51–54] and preclinical data support the emergence of similar resistance mechanisms in the context of PDAC [55, 56]. There is an urgent need to identify additional dependencies of KRAS-driven PDAC and exploit those vulnerabilities as therapeutic targets. DNA-damaging agents (e.g. gemcitabine) are standard-of-care treatments for PDAC. However, innate and acquired chemoresistance limit efficacy of genotoxic therapies [57–59]. It is also critical to elucidate and target chemoresistance mechanisms if we are to curtail the high mortality from PDAC.

Previous studies have highlighted the presence of DDR markers in PDAC samples, supporting a role for oncogene-induced DNA replication stress in the etiology of pancreatic cancer [60]. However, there is no paradigm for how KRAS induces DNA damage during pancreatic carcinogenesis, or how the DDR protects PDAC and their normal precursors from KRAS genotoxicity. To address this knowledge gap, we opted to study consequences of KRAS-induced mitogenesis in normal untransformed human pancreatic nestin-expressing (HPNE) cells [61]. We reasoned that KRAS signaling critically regulates mitogenesis in the pancreatic epithelium [62]. Furthermore, activation of KRAS by mutation in normal pancreatic epithelial cells leads to premalignant lesions termed pancreatic intraepithelial neoplasias [45, 63]. Therefore, the relationships between KRAS and DDR that we define in HPNE will likely be both physiologically and pathologically relevant.

We have developed an experimental system that allows for tight regulation of oncogenic KRAS expression while avoiding artificially high hyper-physiological mitogenic signaling. Using this model system, we identify TRIP13 as an exquisitely specific requirement for DNA synthesis and viability of KRAS-expressing cells. Critically, TRIP13 is pharmacologically tractable and provides opportunities for new therapies that target a unique dependency of KRAS-driven PDAC.

Materials and methods

Cell culture and chemical agents

hTERT-HPNE (ATCC CRL-4023) cells were purchased from the American Type Culture Collection. Pa02c, Pa03c, and hTERT-immortalized HPNE-DT expressing wild-type KRAS or KRAS^{G12V} were provided by Dr Channing Der (UNC). AsPc-1, Panc10.05, and Capan-1 cell lines were purchased from the UNC tissue culture facility. Cells were grown at 37°C in Dulbecco's modified Eagle medium (DMEM) supplemented with 10% tetracycline-negative fetal bovine serum (FBS) and penicillin–streptomycin (1%), in humidified chambers with 5% CO_2. Capan-1 cells were grown in Iscove's modified Dulbecco's medium supplemented with 20% FBS and penicillin–streptomycin (1%). The following drugs were used in this study: doxycycline hydrochloride (Fisher Scientific, BP26531), DCZ0415 (MedChemExpress, HY-130603), olaparib (MedChemExpress, HY-10162), gemcitabine (MedChemExpress, HY-17026), and AZD1775 (MedChemExpress, HY-10993).

LentiCRISPR and sgRNA cloning

To generate knockout cell lines, a blasticidin S deaminase (BSD) selection marker and a destabilization domain (DD) were cloned into lentiCRISPR v2 (Addgene, #52961) via NEBuilder HiFi DNA Assembly in a stepwise manner. BSD cloning was performed by assembling three pieces: two PCR (polymerase chain reaction)-amplified pieces of lentiCRISPR v2 and one PCR-amplified piece of pLX304 (Addgene, #25890) with 13-bp overlaps. LentiCRISPR v2 primers were used to remove puromycin *N*-acetyltransferase selection marker. DD cloning was performed by assembling two pieces: one PCR-amplified piece of lentiCRISPR v2 BSD and one PCR-amplified piece of DD-Cas9 with filler sequence and Venus (Addgene, #90085) with 25-bp overlaps. Small PCR products were purified using a PCR purification kit (QIAGEN, 28104) and large PCR products (>6 kb) were run on a 1% agarose gel and fragments were extracted using a gel extraction kit (QIAGEN, 28706). Fragments were assembled by HiFi DNA Assembly according to manufacturer's instructions (NEB, E2621). Electroporation: 0.75 µl of HiFi assembly mixture was added to 25 µl of electrocompetent bacteria (Lucigen, 60242-2). The bacteria and DNA mixture was electroporated in ice-chilled cuvettes (Bio-Rad, 1652083) using a Gene Pulser Xcell electroporator (Bio-Rad, 1652660) at 1800 V, 10 µF, 600 Ω, and 1 mm cuvette gap. Five hundred microliters of recovery medium was added immediately post-electroporation (Lucigen, 80026-1). Transformed bacteria were incubated at 37°C for 1 h and then plated on LB ampicillin plates and incubated overnight at 37°C. Individual bacterial colonies were transferred to 500 ml LB cultures and incubated at 37°C for 16 h. Cloned plasmid DNA was extracted using plasmid maxiprep kit (QIAGEN, 12362). Oligonucleotides encoding single guide RNA (sgRNA) targeting TRIP13 gene and a nontargeting control sgRNA (see Supplementary Table S1, “Oligo sequences”) were cloned into lentiCRISPR v2 BSD DD-cas9 vector. The resulting vectors were transformed into Endura Chemically Competent Cells according to the manufacturer’s protocol.

Lentivirus generation

To generate lentiviruses for gene knockout or knock-in, replication-incompetent lentivirus was packaged via transfection of HEK293 T cells with either a lentiCRISPR v2 SpCas9 or an LV-mCherry-FLuc (a gift from Shawn Hingtgen, UNC) vector and viral packaging plasmids, pMD2.G and psPAX2, gifts from Didier Trono (Addgene, #12259 and 12260), using a 4:1:3 ratio (12 µg DNA per transfection reaction) with Lipofectamine 2000. One day after the transfection, culture medium was changed. Lentivirus-containing culture medium from transfected cells was collected at 24 and 48 h after medium change, filtered through a 0.45-µm filter, aliquoted, and stored at −80°C.

Lentiviral transduction to generation of stable cell lines

To generate the doxycycline (Dox)-inducible hTERT-HPNE cell lines stably expressing HA-KRAS^{G12V}, the complementary DNA (cDNA) fragment encoding HA-KRAS^{G12V} was PCR amplified from pCGN-HA-K-4B(G12V) [64] and gateway-cloned into the pinducer20 plasmid, which placed it under transcriptional control of a Dox-regulated promoter. High-titer lentivirus was produced in HEK293T cells and hTERT-HPNE cells were infected with lentivirus-containing medium containing 8 mg/ml polybrene (Sigma–Aldrich, TR-1003-G). Medium was changed after 24 h and stably transduced cells were selected by growth in medium containing 1000 mg/ml G418 (Thermo Fisher). To avoid clonal selection of idiosyncratic cells, pools of stably infected cells were used for all experiments. For all HPNE experiments, Dox was replenished every 3 days. To generate *TRIP13* knockout PDAC cell lines, cultures were transduced with lentiviruses (lentiCRISPR v2 SpCas9 sgTRIP13) and then BSD-selected after overnight infection. To generate luciferase-expressing HPNE cell lines, hTERT-HPNE EV and KRAS^{G12V} were transduced with mCherry-FLuc lentiviruses and then sorted on the FACSAria II cell sorter.

3D spheroids

Two thousand cells were grown in ultra-low attachment (ULA) U-bottom 96-well plates (Corning, 650970) with DMEM supplemented with 10% FBS and 1% penicillin–streptomycin for 4 days. For imaging, spheroids were incubated with Hoechst 33342 (Invitrogen, R37605; 1:200; 20 min) in 96-well plates. Propidium iodide was subsequently added to the wells at a final concentration of 8 µg/ml just before imaging. Images as a z-stack were taken using the 10× lens of the Keyence BZ-X800 microscope and were processed using Keyence imaging software. For competitive growth assay, single guide nontargeting and sgTRIP13 cells were mixed with H2B-GFP expressing cells in 1:1 ratio and seeded in 96-well ULA plates for a week. Every two days, half of the medium was replaced with fresh medium. After a week, spheroids were collected in a 15-ml tube, washed with phosphate-buffered saline (PBS), dissociated with Accutase, strained through a 40-µm Nylon cell strainer (Falcon, 352340), and analyzed by a flow cytometer to determine number of GFP-positive and GFP-negative cells. Ratios of GFP-positive and GFP-negative cells were quantified to analyze relative growth. For viability analysis, cells were grown in 96-well ULA plates. Next day, drug was added by replacing half of the medium with fresh medium containing drug. After 3 days of drug treatment, cell viability was assessed using the CellTiter-Glo® 3D Cell Viability Assay.

Immunoblotting

Immunoblotting methods were carried out essentially as described [65–67]. In brief, cells grown in plates were washed thrice in ice-cold PBS and lysed in 100–200 µl of ice-cold cytoskeleton buffer (CSK buffer; 10 mM PIPES, pH 6.8, 100 mM NaCl, 300 mM sucrose, 3 mM $MgCl_2$, 1 mM EGTA, 1 mM dithiothreitol, 0.1 mM ATP, 10 mM NaF, and 0.1% Triton X-100) freshly supplemented with complete protease inhibitor cocktail (Roche, Indianapolis, IN, USA) and PhosSTOP (Roche). In the case of spheroids, they were collected in a 15-ml tube, washed with PBS, and dissociated with Accutase before adding the CSK buffer. Cell lysates were centrifuged at 1500 × *g* for 4 min to remove the CSK-insoluble chromatin fraction. The detergent-insoluble chromatin fractions were washed once with 1 ml of CSK buffer, resuspended in CSK, and treated with nuclease. Cell extracts were separated by sodium dodecyl sulfate–polyacrylamide gel electrophoresis, transferred to nitrocellulose membranes, and incubated overnight with the primary antibodies and 1 h with the secondary antibodies in 5% nonfat milk TBST. The sources of antibodies and dilutions at which they were used are as follows: KRAS (Santa Cruz Biotechnology, sc-30; 1:500); phosphor-p44/42 MAPK (Erk1/2) (Thr202/Tyr204) (Cell Signaling Technology, 9106; 1:1000); HA-tag (Santa Cruz Biotechnology, sc-7392; 1:1000); GAPDH (Santa Cruz Biotechnology, sc-32233; 1:5000); VINCULIN (Sigma–Aldrich, V4505; 1:10 000); phospho-Histone H2A.X (Ser139) (Millipore Sigma, 05-636; 1:5000); PCNA (Santa Cruz Biotechnology, sc-56; 1:500); phosphor RPA32 (S33) (Bethyl, A300-246A; 1:1000); β-actin (Santa Cruz Biotechnology, sc-130656; 1:5000); CDT1 (Bethyl, A300-786A; 1:1000); MCM2 (Santa Cruz Biotechnology, sc-10771; 1:1000); CDC45 (Santa Cruz Biotechnology, sc-9298; 1:1000); TRIP13 (Santa Cruz Biotechnology, sc-514285; 1:500); phospho-ATM(Ser1981) (Santa Cruz Technology, sc-47739; 1:500); ZRANB3 (Bethyl, A303-033A-M; 1:1000); and PRIMPOL (Proteintech, 29824-1-AP; 1:1000). Perkin Elmer Western Lightning Plus ECL was used to develop films.

Population doubling

HPNE cells were counted, seeded, and maintained in the exponential growth phase for 21 days. For subculturing, cells were trypsinized, counted, and re-seeded with or without Dox. Cell counts from three biological replicates were used to calculate population doublings.

RNA interference

For gene knockdown experiments, small interfering RNAs (siRNAs) were reverse transfected using Lipofectamine 2000 according to manufacturer's instructions. Briefly, siRNA oligos were incubated with Lipofectamine 2000 and serum-free OptiMEM for 20 min at room temperature. Trypsinized cells were added directly into the siRNA/OptiMEM/Lipofectamine solution in the plate and were incubated as per individual experimental design. The siRNA sequences are listed in Supplementary Table S1.

Clonogenic assay

Cells were seeded at a density of 2000 cells/well in triplicate in six-well plates. In the case of siRNA experiments, cells were transfected for 24 h before seeding to the plates. Growth medium was replenished every 3 days. For HPNE experiments, Dox was replenished every 3 days. HPNE cells and PDAC cells were allowed to grow for 6 days, except CAPAN-1 that was grown for 9 days. After 6–9 days depending on the cell lines, colonies were stained with 0.05% crystal violet in 1× PBS containing 1% methanol and 1% formaldehyde. The ImageJ plugin ColonyArea was used to automatically quantify stained colonies. The growth curves were generated by normalization to respective control group colony area. The SynergyFinder web application (version 3.0) (https://synergyfinder.fimm.fi/) was used to generate synergy distribution heatmaps.

Cell cycle and BrdU incorporation analysis

Growing cell monolayers were incubated with 10 μM BrdU for 1 h. In experiments with adenovirus, cells were infected with adenoviruses at 1×10^{10} PFU/ml and then cell monolayers were incubated with 10 μM BrdU for 1 h. Cells were washed to remove unincorporated BrdU, trypsinized, and suspended in fixing medium (65% PBS with 35% ethanol) overnight at 4°C. Fixed cells were denatured using HCl and then neutralized with borax before staining with fluorescent anti-BrdU antibodies (FITC mouse anti-BrdU kit; 556028; BD) for half an hour. Nuclei were incubated in PBS containing 10 μg/ml of propidium iodide and 40 μg/ml of RNase A for 1 h. Stained cells were analyzed by flow cytometry on an Accuri C6 flow cytometer (BD) using the manufacturer's software. Replication licensing assay was performed as described previously [68]. BrdU incorporation was calculated by subtracting median BrdU incorporation value for G1-phase cells from median BrdU incorporation value for S-phase cells and normalized to the control group.

Gene expression and survival analysis

For RNA sequencing (RNA-seq), total RNA was isolated from hTERT-immortalized HPNE-DT cells with or without Dox induction of $\text{KRAS}^{\text{G12V}}$ for 6 h using QIAGEN RNeasy (QIAGEN, 74104). Libraries containing 250–300-bp cDNA inserts were polyA selected, prepared, and sequenced on the Illumina platform PE150 by Novogene (Sacramento, CA, USA). The TCGA pancreatic adenocarcinoma (TCGA-PAAD) data were retrieved using TCGAbiolinks R package (version 2.30.0). Samples defined as "high purity" [69] and "treatment-naïve" were used for gene expression analysis. Survival analysis and Kaplan–Meier curves were generated using the original TCGA-PAAD data and were performed using the following R packages: survival (version 3.2-13) and survminer (version 0.4.9).

Mouse tumorigenesis studies

Animal experiments were approved by the Institutional Animal Care and Use Committee at UNC and performed according to guidelines. Suspensions of Pa03c, Pa02c, HPNE EV, and $\text{KRAS}^{\text{G12V}}$ cells at a concentration of 2.5×10^5 cells in 40 μl sterile Matrigel-PBS were injected into the tail of the pancreas of three mice per group with the needle in a direction toward the head of the pancreas using a 0.30 cc syringe and 30 G needle. The needles were held still for 15–20 s to prevent potential leakage. The pancreas was gently placed back into the body cavity and the surgery wound was sutured in layers, clipped, and iodine was applied to prevent infection. 0.1 mg/kg buprenorphine (Buprenex injection, NDC 12496-07575) was injected subcutaneously into each mouse again at 24 h. After the surgery, mice were placed on a heating pad for 5 min to aid in recovery before returning to cage. Mice were monitored daily for three consecutive days after surgery and if required a third dose of buprenorphine was administered. Mice were monitored at least twice weekly. Animals were maintained for up to 6 weeks or until they needed to be euthanized based on humane endpoint criteria. Mouse $\text{KRAS}^{\text{G12V}}$ induction was carried out by Dox-containing water [2 mg/ml, 5% (w/v) sucrose]. Tumor growth was measured weekly using bioluminescence imaging (Revvity, IVIS Lumina III Series and XenoLight D-Luciferin–K^+ Salt Substrate) performed by the UNC Animal Studies Core (see the "Acknowledgements" section). Pancreatic tumors were flash frozen and stored at −80°C. For pathological analysis, tumors were added to molds pre-layered with OCT medium (Tissue-Tek, 62550) for cryofreezing. Cryofrozen OCT blocks were sectioned into 10-μm-thick slices onto Superfrost plus slides (Fisherbrand, 1255015) and stored at −20°C. Slides were stained with hematoxylin and eosin and images were taken at 10× and 2× resolution using a Zeiss microscope.

Iterative indirect immunofluorescence imaging

hTERT-HPNE EV and KRASG12V cells were seeded in glass-bottom 96-well plates treated with poly-L-lysine at 5000 cells/well. Dox induction of KRASG12V was done at the time of seeding at 200 ng/ml. After 3 days of induction, cells were pulse-labeled with EdU (10 μM) for 30 min, fixed with 4% paraformaldehyde (PFA) for 30 min, and then washed three times with DPBS (Corning, 21-031-CV). The blocking, imaging, and elution iterations were done as described in [70]. Briefly, each sample was incubated with 4i blocking solution [100 mM maleimide, 100 mM NH_4Cl, and 1% bovine serum albumin (BSA) in PBS] for 1 h, followed by incubation with diluted primary antibodies overnight at 4°C. After three PBS washes, each sample was incubated with secondary antibodies. Samples were imaged on a Nikon Ti Eclipse microscope. Stitched 8 × 8 images were acquired for each sample using the following filter cubes (Chroma): 4′,6-diamidino-2-

phenylindole (DAPI; 383–408/425/435–485 nm), GFP (450–490/495/500–550 nm), Cy3 (530–560/570/573–648 nm), and Cy5 (590–650/660/663–738 nm). After imaging each protein, samples were washed three times with ddH_2O and then antibodies were eluted and sequentially incubated with the next set of primary antibodies. The antibodies used are as follows: HA (Bethyl, A190-138A); phosphor-ERK (Cell Signaling Technology, 9101); phosphor-H2AX (Cell Signaling Technology, 80312); RB (Cell Signaling Technology, 9309); phosphor-RB (Cell Signaling Technology, 8516); phospho-p53 (S15) (Cell Signaling Technology, 9286); phospho-p21 (T145) (Abcam, ab47300); phospho-p27 (T157) (Abcam, ab805047); and phosphor-CHK1 (Cell Signaling Technology, 12302).

PHATE analysis and visualization

The potential of heat diffusion for affinity-based transition embedding (PHATE) method [71] was applied using the previously mentioned feature set as input variables. The PHATE coordinates, which are data projections, position each cell relative to others based on their molecular signatures as determined by 4i protein markers. PHATE was run on *z*-normalized and filtered features with specific parameters for cell cycle maps [Fig. 1H: *k*-nearest neighbor (knn) = 200, gamma = 1, *n* = 2]. The proliferative cell cycle phases (G1/S/G2/M) in HPNE cells were manually annotated using distinct changes in DNA content. Data were visualized using Python (v3.11.8), numpy (1.26.4), pandas (2.0.3), phate (1.0.11), and Jupyter Notebooks (v2024.2.0). Statistical analysis was performed using one-way analysis of variance (ANOVA) with Tukey's post-hoc test.

DNA fiber analysis of DNA replication dynamics

Growing cells were labeled with 25 μM chloro-deoxyuridine (CldU; C6891; Sigma–Aldrich) for 20 min. Cells were then washed twice with warm medium and immediately labeled with 250 μM iodo-deoxyuridine (IdU; I7125; Sigma–Aldrich) for 20 min. Labeled cells were harvested, washed in PBS, and added to glass slides. Cells were lysed in spreading buffer (200 mM Tris–HCl, pH 7.5, 50 mM EDTA, 0.5% SDS), and DNA fibers were spread across the slide by tilting the slides at an angle. Air-dried DNA fiber slides were fixed in a 3:1 mix of methanol and acetic acid for 10 min. DNA fibers were denatured in 2.5 M HCl for 1 h, incubated in blocking solution (1% BSA, 1% Tween 20 in PBS) for 30 min, and then incubated with mouse anti-BrdU (BD Biosciences, 347583; for IdU detection) and rat anti-BrdU (Abcam, A6326; for CldU detection) primary antibodies for 1 h in the dark. Subsequently, DNA fibers were incubated with secondary antibodies, anti-mouse Alexa Fluor 488 and anti-rat Alexa Fluor 555. Fluorescently labeled DNA fibers were imaged using an Andor Dragonfly Spinning Disk Confocal Microscope (Oxford Instruments, UK) mounted on a Leica DMi8 microscope stand, equipped with an HC PL APO 100×/1.40 OIL CS2 Leica objective. The lengths of CldU (Alexa Fluor 555; red)- and IdU (Alexa Fluor 488; green)-labeled fibers were measured using the ImageJ software, and micrometer values were converted into kilobases using the conversion factor 1 μm = 2.94 kb (1 bp corresponds to ∼340 pm). A minimum of 50 representative DNA fibers were counted for each experimental condition.

Live cell microscopy

To generate hTERT-HPNE cell lines stably expressing GFP-H2B, EV and $KRAS^{G12V}$-HA cells were infected with lentivirus expressing GFP-H2B and selected by growth in medium containing hygromycin B (Thermo Fisher). Cell lines with stable GFP-H2B expression were seeded on Chambered Coverglass from Lab-Tek II (Thermo Fisher, 155382). Cell lines were treated with Dox and transfected with siRNA 24 h before imaging. Time-lapse microscopy was performed on a Keyence BZ-X810 using a 20× objective. Images were taken at 4-min interval for 24 h. Best focus projections of the time series were exported into AVI format. Image sequences were generated using ImageJ and manually quantified.

Immunofluorescence

Two days after siRNA transfection and Dox treatment, HPNE cells were washed twice with PBS, fixed with 2% PFA for 15 min, washed twice with PBS, permeabilized with 0.2% Triton X-100 for 5 min, washed three times with PBS, and blocked with 3% BSA. This was followed by primary antibody (53BP1, sc-22760, 1:200 dilution) incubation for 1 h, three PBS washes, secondary antibody incubation for 1 h, and three washes in PBS. Finally, coverslips were mounted on the slides using fluoroshield with DAPI (#H-1200, Vector Laboratories).

For analysis of 53BP1 foci, high-resolution images were taken using an Andor Dragonfly Spinning Disk Confocal Microscope (Oxford Instruments, UK) mounted in a Leica Dmi8 microscope stand, equipped with an HC PL APO 100×/1.40 OIL CS2 Leica objective. The pinhole size was set to 40 μm, and the camera used was a Zyla Plus 4.2MP sCMOS, featuring a resolution of 2408 × 2048 pixels and an effective pixel size of 0.063 μm. Excitation lasers included a 405-nm laser for DAPI and a 488-nm laser for Alexa Fluor 488. Emission filters used were 445/46 for DAPI and 521/38 for Alexa Fluor 488.

Statistics and reproducibility

Statistical analyses were performed using Microsoft Excel and GraphPad Prism. The Student's *t*-test was used to determine *P*-values for all data involving comparisons between two groups. Results are expressed as the mean ± standard error of the mean or standard deviation of two or more independent experiments as indicated in the legends. The *P*-values are indicated in the figure legends. All biological and biochemical experiments were performed with appropriate internal negative and/or positive controls as indicated.

Results

Establishing an experimental system for defining responses to oncogenic KRAS in normal pancreatic epithelial cells

To model PDAC-relevant oncogenic events, we engineered HPNE cells (TERT-immortalized normal epithelial cell PDAC precursors) to express oncogenic $KRAS^{G12V}$ in a Dox-inducible manner (Fig. 1A). As expected, Dox induction of $KRAS^{G12V}$ expression led to increased phosphorylation of ERK1/2, downstream targets of the KRAS pathway. A Dox dose of 200 ng/ml induced levels of $KRAS^{G12V}$ and pERK comparable to those found in PDAC cell lines (Fig. 1B and C). This level of $KRAS^{G12V}$ expression led to increased cell

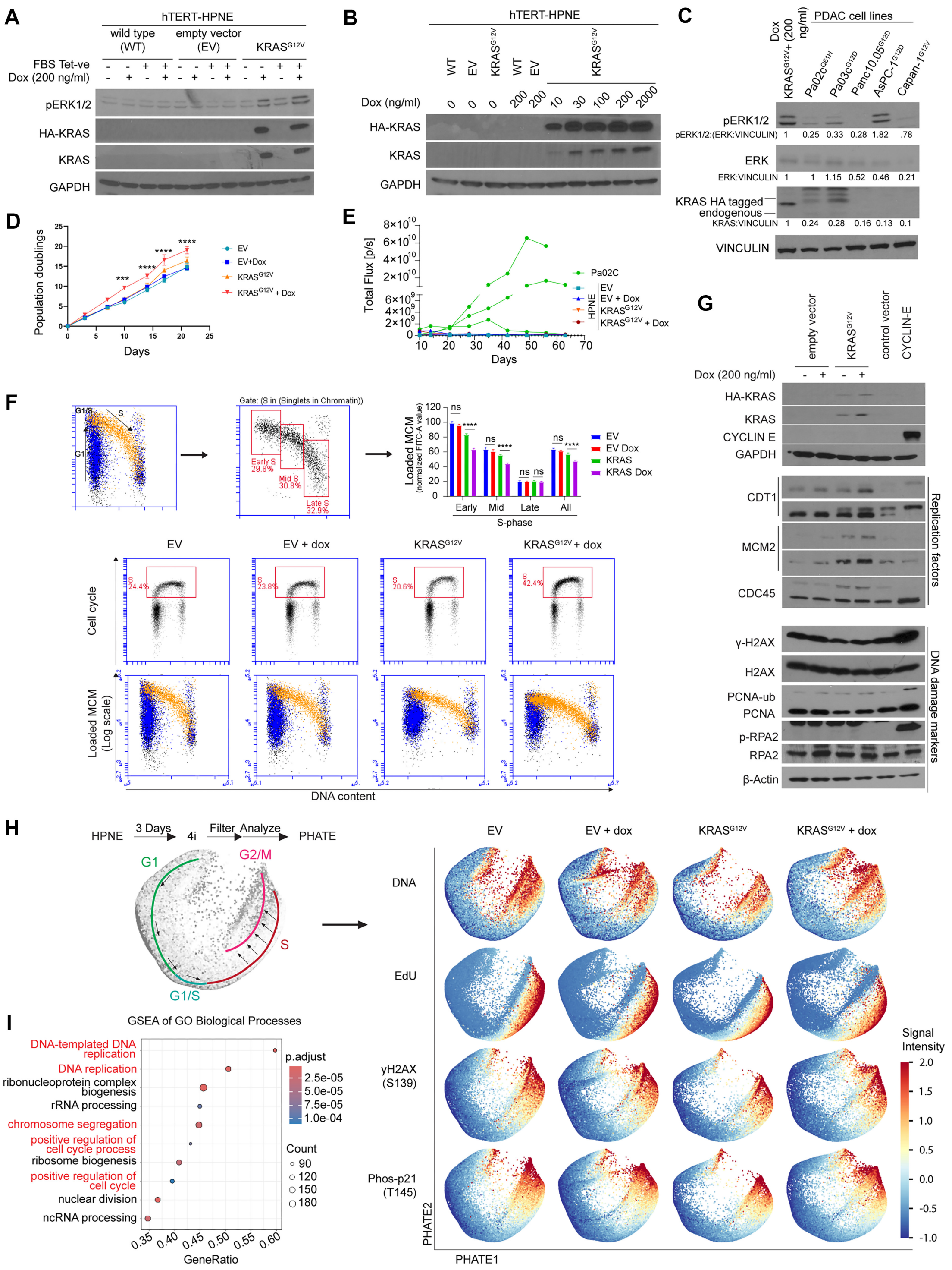

Figure 1. Establishing an HPNE cell system for modeling responses to KRAS-induced DNA replication stress. (**A**, **B**) Immunoblots showing Dox-inducible expression of HA-KRAS^{G12V} and p42/p44 MAPK phosphorylation in HPNE using regular and tetracycline-negative (Tet −ve) FBS. (**C**) Immunoblot showing Dox-inducible p42/p44 MAPK phosphorylation in HPNE and PDAC cell lines. (**D**) Growth curve showing Dox-inducible KRAS^{G12V} expression effect on proliferation. Error bars represent standard deviation (SD) for biological triplicates. Statistical analysis: two-way ANOVA followed by Tukey's multiple comparison test, $*P < .05$, $**P < .01$, $***P < .001$, $****P < .0001$, ns = not significant. (**E**) Plot showing tumor growth of orthotopically implanted HPNE and PDAC cell lines into the pancreas of nude mice ($n = 3$ mice per group). (**F**) Flow cytometry profiles showing the effect of Dox-inducible KRAS^{G12V} expression on BrdU incorporation (middle panels) and chromatin loading of MCM2 (upper panels). The bar charts show quantification of chromatin-loaded MCM (normalized FITC-A value) under the different experimental conditions. Error bars represent SD for biological triplicates. Statistical analysis: two-way ANOVA followed by Tukey's multiple comparison test, $*P < .05$, $**P < .01$, $***P < .001$, $****P < .0001$, ns = not significant. (**G**) Effects of Dox-inducible KRAS^{G12V} or adenovirus-transduced Cyclin E expression on the indicated DNA damage markers and DNA replication factors. HPNE cells were infected with adenovirus-expressing Cyclin E1 (or "empty" control virus) at 1×10^{10} PFU/ml. (**H**) PHATE plots indicating cell cycle trajectories and DNA damage markers of empty vector and KRAS^{G12V}-expressing HPNE and their relevant empty vector controls after 3 days of Dox treatment. (**I**) Gene ontology (GO) analysis of KRAS^{G12V}-induced messenger RNAs (mRNAs) compared to empty vector in HPNE showing top 10 GO terms.

proliferation rates *in vitro* (Fig. 1D). However, when orthotopically implanted into the pancreas of nude mice, KRAS^{G12V}-expressing HPNE cells did not form tumors. In contrast, orthotopically implanted PDAC cell lines readily induced tumor growth (Fig. 1E and Supplementary Fig. S1B–F). Therefore, Dox-induced KRAS^{G12V} expression in HPNE is a model for pre-neoplasia. In flow cytometry experiments, Dox induction of KRAS^{G12V} stimulated cells to enter S phase with reduced levels of minichromosome maintenance (MCM)-loaded chromatin (Fig. 1F), indicating that oncogenic KRAS accelerates G1 at the expense of DNA replication licensing in this system. In contrast with overexpressed Cyclin E (a commonly used oncogene for modeling DNA replication stress), the levels of Dox-induced KRAS^{G12V} expression attained in HPNE did not elicit high levels of DNA replication stress as shown by flow cytometry analysis of BrdU-labeled cells (Fig. 1F and Supplementary Fig. S1A) and DNA damage markers such as γH2AX, PCNA monoubiquitylation, and pRPA as shown by western blot (Fig. 1G and Supplementary Fig. S9).

To ask whether higher resolution analysis would reveal KRAS^{G12V}-induced cell cycle defects in HPNE, we performed iterative indirect immunofluorescence imaging (4i) [70]. As shown in Fig. 1H and Supplementary Fig. S2, our single cell resolution 4i analyses confirmed that KRAS^{G12V} expression induced no major branch points or cell groups. Of the protein markers we examined, only levels of γH2AX (S139) in S phase, phosphorylated TP53 (S15) in G2/M phases, and phosphorylated p27kip (T157) were modestly increased as a result of KRAS^{G12V} expression (Supplementary Fig. S3). We conclude that low levels of KRAS^{G12V} signaling promote proliferation without significantly perturbing the cell cycle or inducing replication stress and DNA damage markers in HPNE.

Using RNA-seq, we confirmed that KRAS^{G12V} expression in HPNE induced a robust transcriptional program, including expression of DNA replication and cell cycle genes (Fig. 1I). Taken together, our results suggest that the DNA replication stress induced by pathologically relevant levels of KRAS^{G12V} signaling is tolerated by HPNE. Therefore, HPNE provides an excellent opportunity to define mechanisms that help tolerate KRAS^{G12V}-induced replication stress.

siRNA screening identifies *TRIP13* as a dependency of KRAS^{G12V}-expressing HPNE cells

Expression of DNA repair genes is often upregulated according to the needs of cells. For example, homologous recombination (HR)-deficient cancers upregulate POLQ, a DNA polymerase that mediates a backup DNA repair mechanism needed to tolerate HR deficiency [72]. By analogy, we hypothesized that cells expressing KRAS^{G12V} might upregulate genome maintenance factors involved in tolerating KRAS-induced DNA replication stress. Therefore, we used RNA-seq data to identify DDR genes (Supplementary Table 3, gene list) that were differentially expressed [adjusted P-value $<.05$; absolute $\log_2$ fold change (FC) >0.5] between control and KRAS^{G12V}-expressing HPNE. As shown in Fig. 2A, KRAS^{G12V} expression resulted in 109 and 26 DDR genes being upregulated and downregulated, respectively. We also interrogated gene expression data for TCGA-PAAD and identified 43 and 17 DDR genes being upregulated and downregulated in primary KRAS-mutated tumors when compared with normal pancreas (Fig. 2B). The heatmaps in Fig. 2C and D show the relative expression levels of DDR genes that were upregulated in KRAS^{G12V}-expressing HPNE cells (when compared with parental HPNE) and KRAS-mutant pancreatic cancers (when compared with normal pancreatic tissue). Fifteen of the DDR genes that were upregulated following KRAS^{G12V} induction in HPNE cells were also expressed at high levels in KRAS-mutant pancreatic tumors (Fig. 2E). The DDR genes that were upregulated in both mutant KRAS-expressing groups are marked with an asterisk in Fig. 2C and D. We generated a library of siRNAs targeting 17 of the DDR genes that were upregulated in KRAS^{G12V}-expressing HPNE (ARID1A, BRCA2, CDCA7L, FANCI, HELLS, MCM6, RAD54B, RNF168), in mutant KRAS-expressing pancreatic tumors (MNAT1, TK1, SMYD3), or in both groups (AURKA, CDC6, MELK, PLK1, RAD51, TRIP13). Using the resulting siRNA library (which targets KRAS-inducible and PDAC-associated DDR mRNAs), we screened for genes that were required for cell viability and ongoing DNA synthesis only in KRAS-active HPNE. The experimental workflow for our screen is depicted in Fig. 3A. Figure 3B summarizes our screen results and provides an aerial view of how the DDR-directed siRNAs in our library affected survival and ongoing DNA synthesis of EV-HPNE and KRAS^{G12V}-HPNE ± Dox.

Our screening experiments identified *TRIP13* as a requirement for both clonogenic survival and ongoing DNA synthesis in KRAS^{G12V}-expressing HPNE but not in control HPNE lacking mutant KRAS (Supplementary Fig. S4A–C). In secondary validation experiments, KRAS^{G12V} expression led to more than two-fold increase in clonogenic survival in HPNE treated with a control siRNA (Fig. 3C). However, in TRIP13-ablated cells, KRAS induction led to around five-fold decrease in clonogenic survival (Fig. 3C). Our flow cytometry analyses showed that TRIP13 depletion led to reduced DNA synthesis rates only in KRAS^{G12V}-expressing HPNE (Fig. 3D). We validated the role of TRIP13 in averting DNA replication stress using four independent siRNAs targeting TRIP13 (Fig. 3E). We conclude that TRIP13 is specifically required for DNA synthesis and viability of HPNE expressing oncogenic KRAS. We asked whether TRIP13 is also important for tolerating replication stress induced by other oncogenes. As shown in Supplementary Fig. S5A–D, TRIP13 depletion also led to reduced DNA synthesis and decreased cell viability in HPNE cells in which we ectopically expressed Cyclin E or MYC oncogenes. Based on our analysis with representative important human oncogenes (KRAS, Cyclin E, MYC), we suggest that TRIP13 may have broad roles in sustaining DNA synthesis and viability of oncogene-expressing cells.

Next, we determined the relationship between TRIP13 expression and KRAS–ERK signaling in cancer. Klomp *et al.* recently performed transcriptional profiling of a large panel of cell lines and PDX models in which KRAS/ERK signaling was conditionally ablated to define a KRAS/ERK-dependent gene signature [73]. We interrogated the transcriptome data generated by Klomp *et al.* to test relationships between TRIP13 expression and KRAS/ERK signaling. As shown in Fig. 3F, conditional ablation of KRAS/ERK signaling was associated with reduced *TRIP13* expression in all datasets. In a TCGA cohort of PDAC patients, high TRIP13 expression (upper quartile) was associated with reduced survival probability (Fig. 3F). Interestingly, the correlation between high TRIP13 expression and reduced survival was evident only in male patients (Fig. 3F and Supplementary Fig. 5E). These clinical data are also potentially consistent with a role for TRIP13 in sustaining tumors harboring oncogenic KRAS.

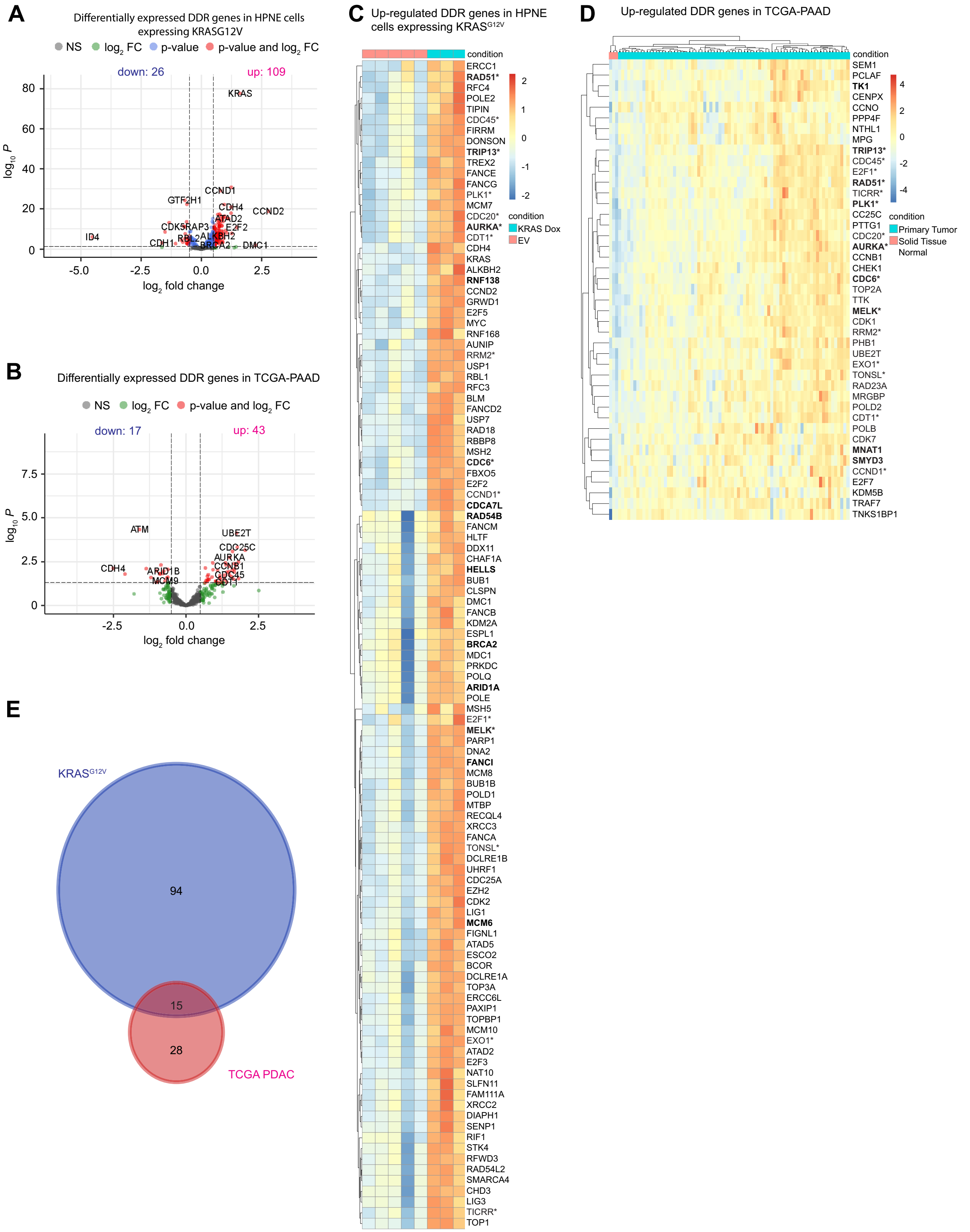

Figure 2. Analysis of the HPNE transcriptome reveals KRAS-inducible DDR genes. (**A**) Volcano plot showing log$_2$FC in mRNA expression of DDR genes against $-\log_{10}$ adjusted *P*-value for hTERT-HPNE expressing KRAS^{G12V} against control with wild-type KRAS. (**B**) Volcano plot showing log$_2$FC in mRNA expression of DDR genes against $-\log_{10}$ adjusted *P*-value for TCGA-PAAD primary tumors against solid tissue normal pancreas. (**C**) Heatmap showing upregulated DDR genes in hTERT-HPNE expressing KRAS^{G12V} against control with wild-type KRAS. (**D**) Heatmap showing upregulated DDR genes in TCGA-PAAD primary tumors against solid tissue normal pancreas. (**E**) Venn diagram showing the numbers of upregulated DDR genes in hTERT-HPNE expressing KRAS^{G12V} and TCGA-PAAD primary tumors, and overlap between them (15 upregulated DDR genes common between hTERT-HPNE expressing KRAS^{G12V} and TCGA-PAAD primary tumors are marked with an asterisk; and genes chosen for the siRNA screen are indicated in bold).

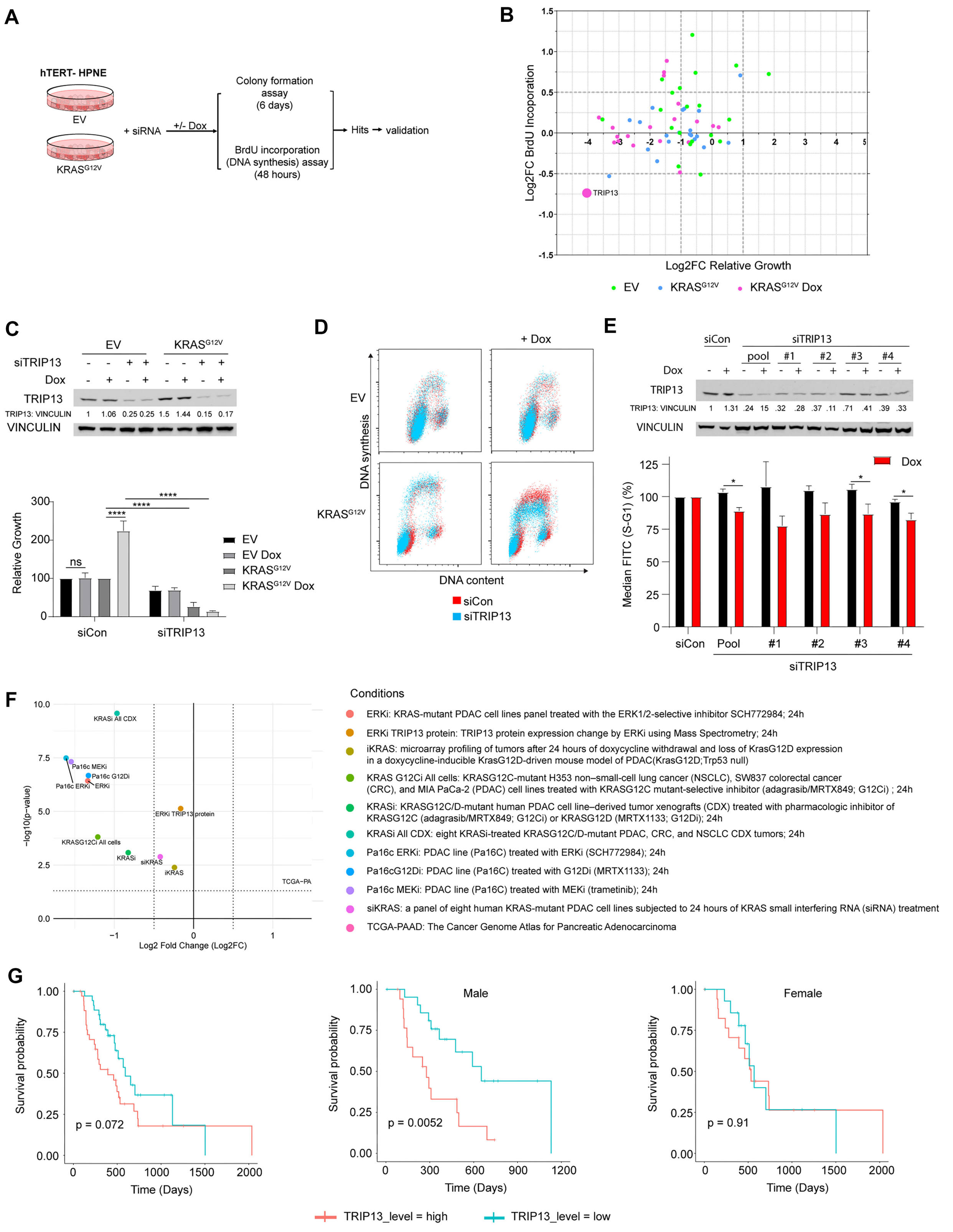

Figure 3. siRNA screening identifies TRIP13 as a dependency of KRAS-expressing HPNE. (**A**) Experimental workflow of siRNA screen for DDR dependencies of KRAS^{G12V}-expressing HPNE. (**B**) Plot showing effect of library siRNAs on clonogenic survival and BrdU incorporation of empty vector and KRAS^{G12V}-expressing HPNE. (**C**) Immunoblot validating siRNA-mediated knockdown of TRIP13 (upper panel) and bar chart showing effect of TRIP13 knockdown on clonogenic survival in empty vector and KRAS^{G12V}-expressing HPNE. Error bars represent SD for biological triplicates. Statistical analysis: two-way ANOVA followed by Tukey's multiple comparison test, $*P < .05$, $**P < .01$, $***P < .001$, $****P < .0001$, ns = not significant. (**D**) Flow cytometry plots showing effect of TRIP13 siRNA on cell cycle profiles and BrdU incorporation in empty vector and KRAS^{G12V}-expressing HPNE. (**E**) Results of immunoblot (upper panel) and flow cytometry analyses (lower panel) showing effect of multiple independent TRIP13-directed siRNAs on BrdU incorporation in KRAS^{G12V}-expressing HPNE. Error bars represent SD for biological triplicates. Statistical analysis: Student's *t*-test, $*P < .05$, $**P <$ .01, $***P < .001$, $****P < .0001$, ns = not significant. (**F**) Volcano plot showing effects of KRAS and ERK status on TRIP13 expression. (**G**) Kaplan–Meier curves showing overall survival of TRIP13 expression in TCGA-PAAD.

TRIP13 sustains DNA replication in KRAS-expressing cells via the HR pathway

The reduced DNA synthesis rates that we observed in TRIP13-ablated cells expressing oncogenic KRAS could potentially be due to changes in replication fork velocity or altered origin firing. To distinguish between these mechanisms, we investigated the role of TRIP13 in DNA replication dynamics using DNA fiber analysis. As shown in Fig. 4A, TRIP13 depletion led to reduced DNA replication fork speeds specifically in KRAS^{G12V}-expressing cells. Loss of TRIP13 in KRAS^{G12V}-expressing cells also led to an increase in numbers of stalled forks (Supplementary Fig. S6), but did not significantly reduce new origin firing.

Next, we considered the potential mechanisms by which TRIP13 facilitates replication fork movement. TRIP13 is an AAA+ ATPase that regulates the cell cycle and genome maintenance factors MAD2 and REV7 [74]. Mechanistically, TRIP13 converts MAD2 and REV7 from "closed" to "open" conformations dissociating them from their binding partners. TRIP13-mediated dissociation of MAD2 and REV7 complexes inhibits translesion synthesis (TLS; a damage-tolerant mode of DNA synthesis), promotes HR, and relieves inhibition of mitotic progression. TRIP13 ablation is expected to promote Polζ-mediated TLS, inhibit HR, and relieve APC inhibition to promote mitotic progression. Therefore, we systematically tested whether increased TLS, reduced HR, or changes in mitotic exit accounted for the TRIP13 dependency of KRAS^{G12V}-expressing cells.

First, we performed epistasis analysis to investigate the relationship between TRIP13 and HR factors in KRAS^{G12V}-expressing cells. We used siRNA to knock down key factors in the HR pathway (BRCA1, BRCA2, and PALB2) individually or in combination with TRIP13, and then determined the impact of these ablations on clonogenic survival of control or KRAS^{G12V}-expressing cells. As shown in Fig. 4B, knockdown of BRCA1, BRCA2, or PALB2 phenocopied the survival defects of TRIP13-depleted cells. Moreover, co-depletion of TRIP13 with BRCA1, BRCA2, or PALB2 did not lead to additive effects on colony survival. The results of Fig. 4B suggest that TRIP13 participates in the same pathway as BRCA1, BRCA2, or PALB2 to maintain HR and promote survival of KRAS^{G12V}-expressing cells. HR-compromised cells are typically sensitive to poly-ADP ribose polymerase (PARP) inhibitors [75]. As shown in Fig. 4C, TRIP13-depleted cells were sensitized to the PARP inhibitor olaparib in a KRAS^{G12V}-dependent manner, further indicating that TRIP13 sustains KRAS^{G12V}-expressing cells via an HR-mediated mechanism.

Interestingly, TRIP13 knockdown also led to reduced numbers of nuclear 53BP1 foci across all of our HPNE cell lines (Supplementary Fig. S7A), suggesting that TRIP13 may also have a role in promoting nonhomologous end joining (NHEJ), as also suggested by other investigators [76, 77]. However, based on the epistatic relationship between TRIP13 and HR genes (Fig. 4B), we infer that the role of TRIP13 in HR is most important for promoting tolerance of KRASG12V-induced replication stress.

Next, we tested whether the effect of TRIP13 depletion on survival of KRAS^{G12V}-expressing cells was mediated via TLS. We reasoned that if excessive TLS due to accumulation of REV7–REV3 complexes accounts for the survival defects of TRIP13-depleted (KRAS^{G12V}-expressing) cells, these defects should be rescued by TLS inhibition. Therefore, we used the REV1 inhibitor JH-RE-06 [78] to inhibit TLS in KRAS^{G12V}-expressing HPNE cells that were conditionally treated with TRIP13 siRNA. Interestingly, TLS inhibition did not rescue the reduced viability of TRIP13-depleted KRAS^{G12V}-expressing cells (Fig. 4C). On the contrary, JH-RE-06 treatment further reduced viability of TRIP13-deficient cells expressing oncogenic KRAS (Fig. 4C). We conclude that the sensitivity of TRIP13-depleted cells to oncogenic KRAS is not caused by excessive TLS. Instead, we infer that the HR deficiency of TRIP13-depleted cells leads to increased dependency on TLS to facilitate tolerance of KRAS^{G12V}-induced DNA replication stress.

Finally, to determine whether the survival defects of TRIP13-depleted cells expressing KRASG12V were mediated via dysregulation of the mitotic MAD2B–APC signaling axis, we directly measured mitotic progression using live cell imaging. We generated HPNE and HPNE-KRAS^{G12V} cells stably expressing a GFP-histone construct, treated the resulting cells conditionally with TRIP13 siRNA, and visualized chromosome dynamics over a 24-h period. Movies were analyzed and fate maps were generated for all experimental conditions. As shown in Fig. 4D, TRIP13 depletion in KRAS^{G12V}-expressing cells did not affect mitotic timing or post-mitotic fates of dividing cells. We conclude that TRIP13 does not significantly affect MAD2/APC function or mitotic exit in KRAS^{G12V}-expressing cells. Instead, TRIP13 promotes survival of KRAS^{G12V}-expressing cells by maintaining HR.

TRIP13 is a dependency of established PDAC cells

Because our experiments with a pre-neoplasia model showed that TRIP13 sustains KRAS^{G12V}-expressing cells, we next asked whether TRIP13 was also necessary for survival of established PDAC cells expressing oncogenic KRAS. Therefore, we investigated the TRIP13 dependency of a panel of five established PDAC cell lines, including HR-deficient (HRD) CAPAN-1 cells. As shown in Fig. 5A and B, treatment with TRIP13 siRNA suppressed clonogenic survival and DNA synthesis of HR-sufficient PDAC cell lines (AsPc-1, Panc10.05, Pa02C, and Pa03C). However, clonogenic survival and DNA synthesis of BRCA2-deficient CAPAN-1 cells were relatively insensitive to TRIP13 depletion (Fig. 5A and B).

In the HR-sufficient PDAC cell lines, clonogenic survival was reduced after treatment with the TRIP13 inhibitor DCZ0415 (Fig. 5C). However, clonogenic survival of HR-deficient CAPAN-1 cells was relatively resistant to pharmacological inhibition of TRIP13 (Fig. 5C). Similar to our results with DCZ0415 treatment, genetic ablation of *TRIP13* (using sgRNA) led to reduced proliferation of Pa02c and Pa03c PDAC cell lines (Fig. 5D). We recently reported that cancer cells in 3D culture (which recapitulate hallmark characteristics of tumors more closely than cells in monolayer culture) often have different requirements for stress tolerance [79]. Therefore, we established conditions for growing Pa02c and Pa03c cells in 3D culture. As shown in Fig. 5E, both PDAC cell lines seeded in ULA plates organized into 3D spheroid structures with radial gradients of proliferation and death that mimic how cells organize in tumors. As expected from our previous work [79], immunoblotting of cell extracts revealed differences in expression of cancer stemness markers between 2D and 3D cultures of PDAC cells (Fig. 5E). Interestingly, in both Pa02c and Pa03c cell lines, KRAS expression was elevated during 3D growth when compared with monolayers.

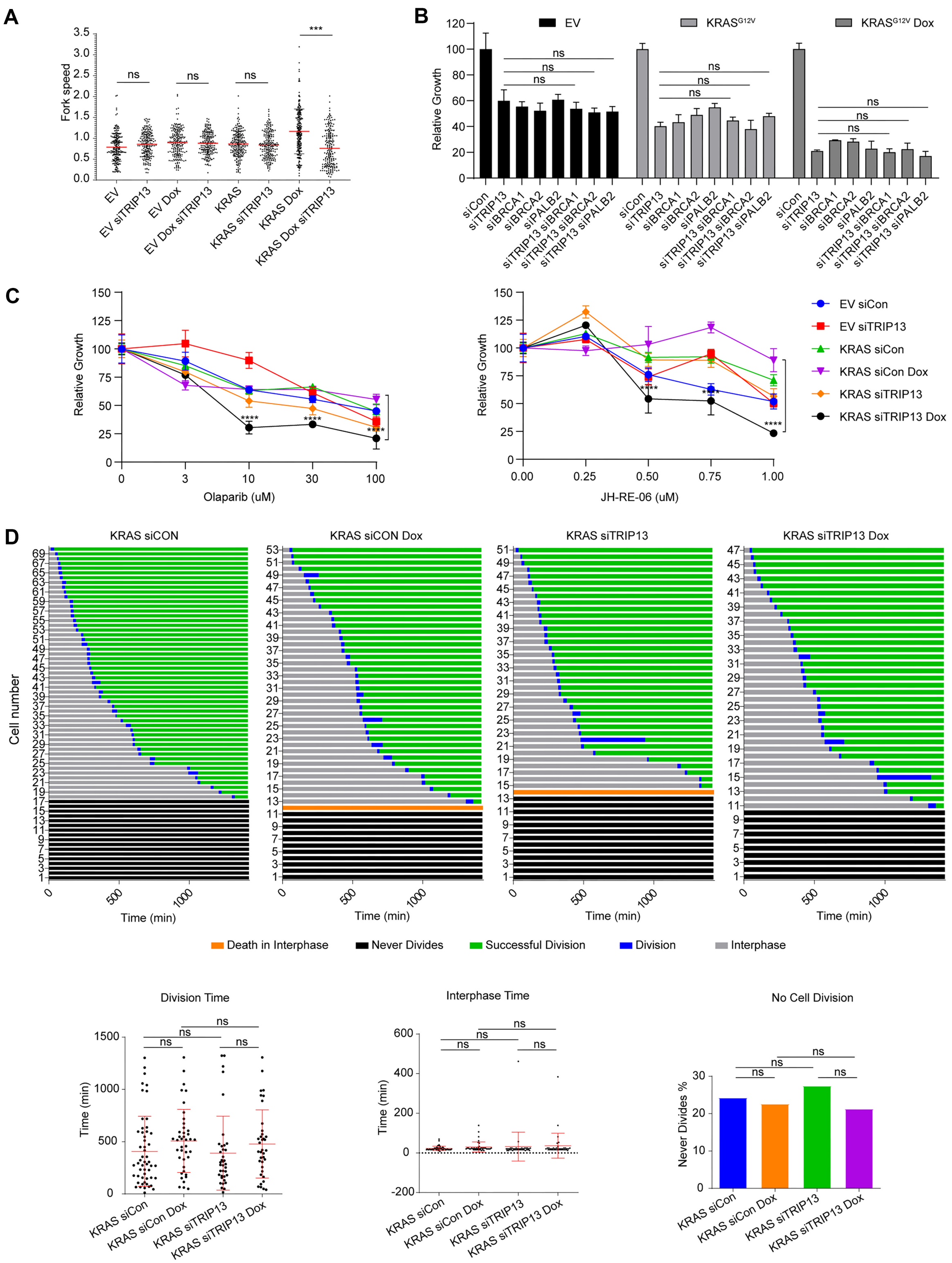

Figure 4. TRIP13 is epistatic with HR genes for tolerance of KRAS-induced DNA replication stress in HPNE cells. (**A**) Results of DNA fiber assays showing effects of KRAS^{G12V} expression and TRIP13 knockdown on DNA replication fork velocities in HPNE. Error bars represent SD for biological triplicates. Statistical analysis: one-way ANOVA followed by Tukey's multiple comparison test, $^{*}P < .05$, $^{**}P < .01$, $^{***}P < .001$, $^{****}P < .0001$, ns = not significant. (**B**) Bar chart showing effects of siRNAs against TRIP13, BRCA1, BRCA2, and PALB2 on colony survival assays in empty vector and KRAS^{G12V}-expressing HPNE. Error bars represent SD for triplicate. Statistical analysis: one-way ANOVA followed by Tukey's multiple comparison test, $^{*}P < .05$, $^{**}P < .01$, $^{***}P < .001$, $^{****}P < .0001$, ns = not significant. (**C**) Results of clonogenic survival assays showing dose-dependent effects of olaparib (left panel) and JH-RE-06 (right panel) on viability of empty vector and KRAS^{G12V}-expressing HPNE. Error bars represent SD for triplicate. Statistical analysis: two-way ANOVA followed by Tukey's multiple comparison test, $^{*}P < .05$, $^{**}P < .01$, $^{***}P < .001$, $^{****}P < .0001$, ns = not significant. (**D**) Results of live cell imaging showing mitotic fates of control and Dox-induced KRAS^{G12V}-HPNE cells. Error bars represent SD for biological triplicates. Statistical analysis: two-way ANOVA followed by Tukey's multiple comparison test, $^{*}P < .05$, $^{**}P < .01$, $^{***}P < .001$, $^{****}P < .0001$, ns = not significant.

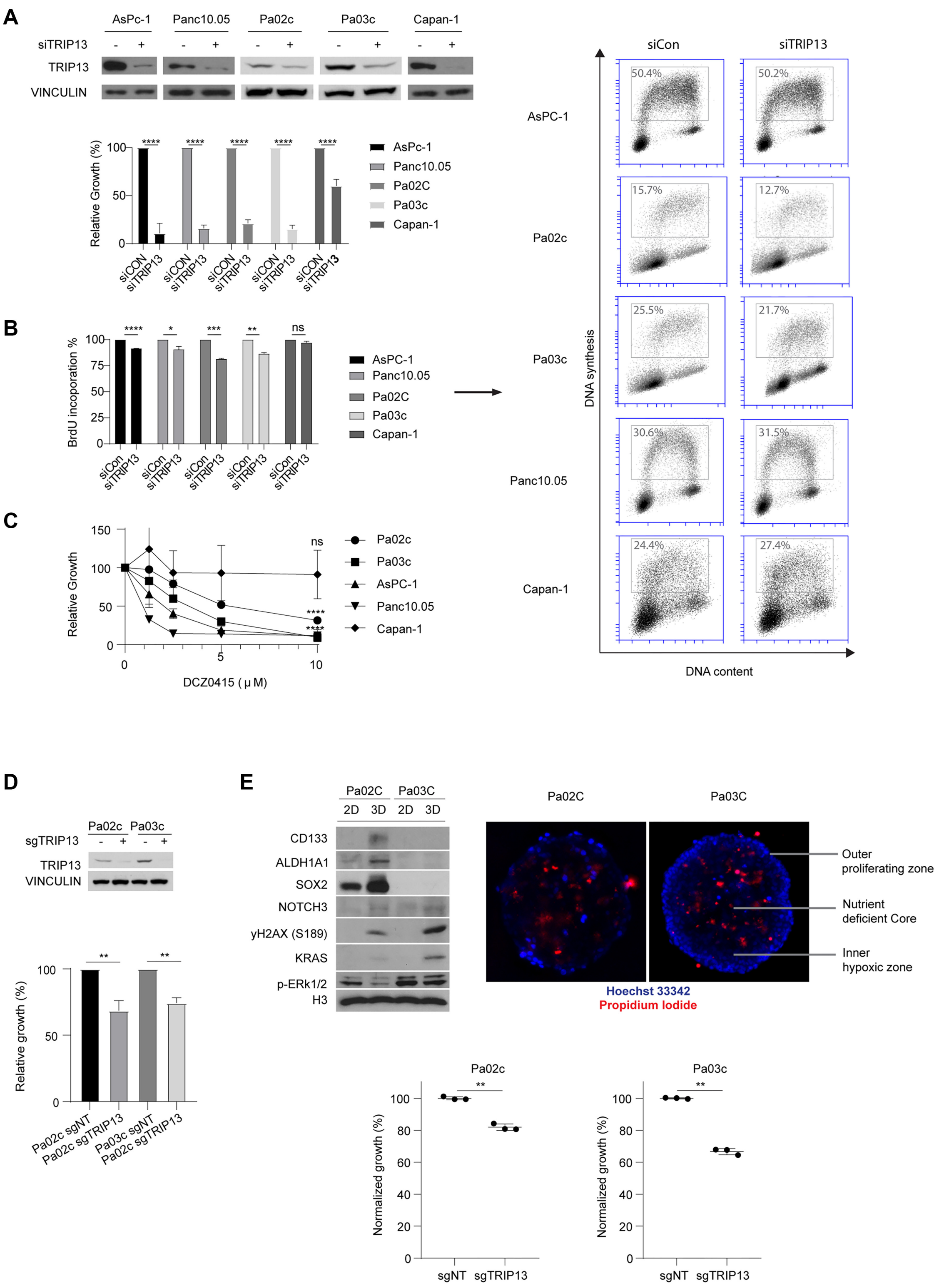

Figure 5. PDAC cell lines require TRIP13 for survival and DNA synthesis. (**A**) Immunoblots validating TRIP13 knockdown using siRNA in PDAC cell lines (upper panel) and effects of TRIP13 siRNA on clonogenic survival of PDAC cells (lower panel). Error bars represent SD for triplicate. Statistical analysis: Student's *t*-test, **P* < .05, ***P* < .01, ****P* < .001, *****P* < .0001, ns = not significant. (**B**) Effect of TRIP13 siRNA on cell cycle distribution and BrdU incorporation in PDAC cell lines. Error bars represent SD for triplicate. Statistical analysis: two-way ANOVA followed by Tukey's multiple comparison test, **P* < .05, ***P* < .01, ****P* < .001, *****P* < .0001, ns = not significant. (**C**) Dose-dependent inhibition of clonogenic survival by DCZ0415 in PDAC cell lines. Error bars represent SD for triplicate. Statistical analysis: Student's *t*-test, **P* < .05, ***P* < .01, ****P* < .001, *****P* < .0001, ns = not significant. (**D**) Immunoblots validating TRIP13 knockdown using siTRIP13 in PDAC cell lines (upper panel) and effects of sgTRIP13 on clonogenic survival of PDAC cells (lower panel). Error bars represent SD for triplicate experimental samples. Statistical analysis: Student's *t*-test, **P* < .05, ***P* < .01, ****P* < .001, *****P* < .0001, ns = not significant. (**E**) The upper panels show immunofluorescence microscopy images of 3D spheroids of PDAC cell lines and immunoblots comparing expression levels of the indicated proteins between 2D and 3D cultures. The lower panel shows the effect of sgTRIP13 treatment on the growth of PDAC cells in spheroid culture as determined using a GFP competitive growth assay.

Consistent with the results of our previous experiments using monolayer cultures, *TRIP13* ablation (using sgRNA) also led to reduced viability of Pa02c and Pa03c cells in 3D culture (Fig. 5E). Increasingly, spheroid and "tumorsphere" culture is being adopted as a preclinical model. The results of Fig. 5E strengthen the notion that TRIP13 is important for PDAC cells to grow as organized and pathologically relevant 3D structures.

TRIP13 confers resistance to therapeutic DNA-damaging agents

Next, we asked whether *TRIP13* loss can also be leveraged as a vulnerability to enhance sensitivity to therapeutic agents. Similar to KRAS^{G12V}-expressing HPNE cells, *TRIP13*$^{-/-}$ Pa02c and Pa03c PDAC cell lines (Supplementary Fig. S5B) displayed a hallmark *BRCA*-ness phenotype, namely PARPi sensitivity (Fig. 6A). Recent work suggests that *BRCA* deficiencies lead to accumulation of extensive single-stranded DNA (ssDNA) in the genome [80]. Therefore, we predicted that *TRIP13* deficiency would lead to a dependency on TLS-mediated ssDNA gap filling. Consistent with this prediction, *TRIP13*$^{-/-}$ PDAC cells were sensitive to the TLS inhibitor JH-RE-06 (Fig. 6A). *TRIP13* deficiency also sensitized PDAC cells to gemcitabine (a first-line therapy for pancreatic cancer) and the WEE1 inhibitor AZD1775 (which has been explored as a potential treatment for PDAC) (Fig. 6A). The olaparib and JH-RE-06 sensitivities of *TRIP13*-PDAC cell lines were evident when we performed these experiments using multiple platforms, including clonogenic assays (Fig. 6A), CellTiter-Blue® Cell Viability Assays (Fig. 6B), and 3D spheroid cultures (Fig. 6C). Taken together, these experiments demonstrate the robustness of the synergy between TRIP13 deficiency and TLS or PARP inhibition.

As expected from our studies with genetic ablation of *TRIP13*, the pharmacological TRIP13 inhibitor (DCZ0415) also synergized with JH-RE-06 or gemcitabine to kill HR-sufficient PDAC cell lines (Fig. 6D and Supplementary Fig. S8). However, in the HR-deficient CAPAN-1 PDAC cell line, we observed no synergy or mild antagonism between DCZ0415 and JH-RE-06 or gemcitabine. Therefore, we conclude that the sensitivity of TRIP13-ablated (or TRIP13 inhibitor-treated) cells to JH-RE-06 and gemcitabine is due to reduced HR activity.

The lethality of therapeutic agents to HR-compromised cells has been attributed to both DNA double strand break (DSB) and ssDNA gaps [80]. The extent to which each DNA lesion contributes to cell death remains heavily debated and may differ depending on biological context. To understand the molecular underpinnings of JH-RE-06 and gemcitabine sensitivities in the setting of TRIP13-depleted PDAC, we measured the accumulation of ssDNA and DSB markers in PDAC cells treated with JH-RE-06 or gemcitabine.

In HR-sufficient AsPC-1 and Pa03C cells, JH-RE-06 treatment induced accumulation of the DSB marker pATM (S1981) only after TRIP13 depletion (Fig. 6C). In contrast, in HR-deficient CAPAN-1 cells, pATM (S1981) was induced to high levels by JH-RE-06 treatment in both control and TRIP13-depleted cultures (Fig. 6C). These results suggest that HR defects resulting from TRIP13 depletion (in AsPC-1 or Pa03C cells) or from intrinsic HR defects (in CAPAN-1 cells) create a dependency on TLS for eliminating ssDNA gaps and averting DSB formation. Interestingly, in immunofluorescence microscopy analyses, we observed that TRIP13 knockdown led to reduced levels of nuclear 53BP1 foci, both in untreated and in JH-RE-06 treated cells (Supplementary Fig. S7B). This result suggests that TRIP13 may also promote NHEJ in PDAC cells and that the synergistic lethality caused by TRIP13 loss in combination with JH-RE-06 may be driven by multiple mechanisms, including HR and NHEJ defects.

The patterns of compensatory DSB signaling induced by gemcitabine in TRIP13-depleted cells were very different from those induced by JH-RE-06. Gemcitabine induced similar levels of pATM (S1981) in control and TRIP13-depleted cultures of AsPC-1 and Pa03C cells (Fig. 6C). However, in HR-deficient CAPAN-1 cells, gemcitabine induced a larger increase in pATM (S1981) levels in TRIP13-depleted cultures when compared with control cultures (Fig. 6C). We observed similar patterns for chromatin binding of ZRANB3 and PRIMPOL (which mediates template switching and repriming in response to replication fork stalling) in CAPAN-1 cells: gemcitabine-induced levels of both ZRANB3 and PRIMPOL on chromatin increased more in TRIP13-depleted cells than in control (TRIP13-replete) cultures. These results indicate that the role of TRIP13 in promoting tolerance of gemcitabine-induced DNA lesions is not mediated solely via HR.

Discussion

Oncogene-induced DNA replication stress has been studied using a limited number of representative oncogenes such as *CCNE1*, typically expressed at very high levels in pathologically irrelevant cell lines such as U2OS or fibroblasts. Here, we have established a new pre-neoplasia model in which oncogenic KRAS is expressed at pathologically relevant levels in precursor cell line that is appropriate for PDAC. Using this more pathologically relevant model system, we find that low-level KRAS expression is mitogenic, yet does not significantly induce replication stress, senescence, or major disruptions (such as the remarkable whole genome duplication that results when *CCNE1* is massively overexpressed in U2OS cells) [29]. Using a comparison of our Dox-inducible KRAS^{G12V} model and KRAS-mutant PDAC patient RNA-seq data followed by a candidate gene approach, we identified TRIP13 as a new mediator that allows HPNE to tolerate the DNA replication stress caused by low-level oncogenic KRAS.

TRIP13 targets multiple protein complexes in the DDR and cell cycle, including REV7–Shieldin, REV7–TLS, REV7/MAD2B–APC, and likely others. In the setting of untransformed HPNE cells expressing oncogenic KRAS, the role of TRIP13 in sustaining DNA synthesis and viability is most readily explained by its ability to promote HR. This conclusion is suggested both by the epistatic relationship between TRIP13 and HR genes for tolerating *KRAS*^{G12V} expression and by our observation that TRIP13 ablation in KRAS^{G12V}-expressing HPNE induces a hallmark HRD phenotype, namely PARPi sensitivity. In addition to PARPi sensitivity, HRD can create a dependency on TLS for gap filling [81]—a feature that fully explains JH-RE-06 sensitivity of TRIP13-depleted cells that express KRAS^{G12V}. HR contributes to tolerance of replication stress induced by other oncogenes, including CCNE1 [82] and β-catenin [27]. Moreover, TRIP13 is overexpressed in many cancers [83]. Therefore, it will be interesting to determine whether TRIP13 induction in malignant cells is a general adaptive response to diverse forms of oncogene-induced DNA replication stress.

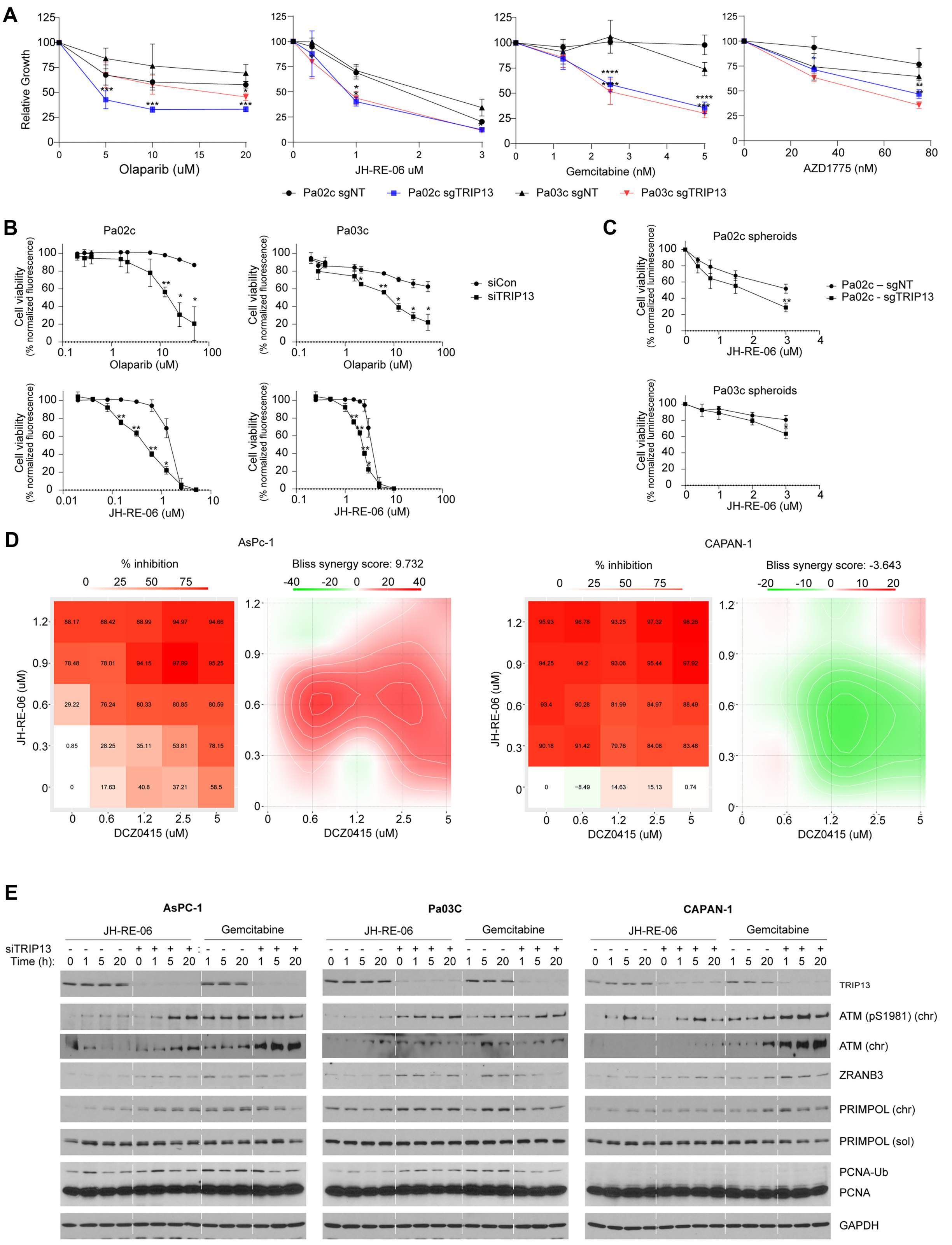

Figure 6. TRIP13 loss sensitizes PDAC cell lines to therapeutic agents. (**A**) Dose-dependent effects of pharmacological agents (JH-RE-06, gemcitabine, olaparib, and AZD1775) on clonogenic survival of Pa02C and Pa03C cells after conditional treatment with TRIP13 siRNA. Error bars represent SD for triplicate. Statistical analysis: Student's *t*-test, $*P < .05$, $**P < .01$, $***P < .001$, $****P < .0001$, ns = not significant. (**B**) Results of CellTiter-Blue® assays showing dose-dependent effects of pharmacological agents (JH-RE-06 and olaparib) on viability of Pa02C and Pa03C cells after conditional treatment with TRIP13 siRNA. Error bars represent SD for biological duplicates. Statistical analysis: *t*-test, $*P < .05$, $**P < .01$, $***P < .001$, $****P < .0001$, ns = not significant. (**C**) Results of CellTiter-Blue® assays showing dose-dependent effects of JH-RE-06 on viability of Pa02C and Pa03C 3D cells in spheroid culture after conditional treatment with sgTRIP13. Error bars represent SD for biological duplicates. Statistical analysis: *t*-test, $*P < .05$, $**P < .01$, $***P < .001$, $****P < .0001$, ns = not significant. (**D**) Synergy maps and synergy scores showing multi-dose combination effects of DCZ0415 and JH-RE-06 on clonogenic survival of AsPc-1 and Capan-1 cells. (**E**) Immunoblots showing expression levels of the indicated DDR markers in control and TRIP13 siRNA-treated PDAC cell lines at different times after treatment with JH-RE-06 or gemcitabine.

In addition to its role in allowing neoplastic cells to tolerate KRAS^{G12V} (and perhaps other oncogenes), we show that TRIP13 also allows PDAC cells to tolerate therapeutic agents, including the PARP inhibitor olaparib. Interestingly, however, the impact of TRIP13 on PARPi sensitivity appears to be context-dependent. For example, we show that TRIP13 knockdown does not increase olaparib sensitivity of HR-deficient Capan-1 PDAC cells, indicating that in these cells the role of TRIP13 in resisting PARP inhibitors is HR-dependent. In contrast, TRIP13 depletion led to increased olaparib sensitivity in BRCA1-deficient SUM149PT breast cancer cells [84]. Paradoxically, TRIP13 depletion did not affect olaparib sensitivity in wild-type RPE, yet TRIP13 loss (using shRNA and sgRNA) rendered BRCA1-deficient RPE less sensitive to olaparib [85]. Most likely, the variability of olaparib sensitivity phenotypes caused by TRIP13 loss reflects the pleiotropic roles of TRIP13 in DNA repair. Since DDR features can vary tremendously between different cancer cells, the mechanisms by which TRIP13 modulates the DDR are likely to vary significantly depending on cellular background.

In addition to the well-studied complexes of REV7 with REV3 (which promotes TLS) and shieldin (which is inhibitory for resection and HR), REV7 also associates with chromosome alignment-maintaining phosphoprotein 1 or CHAMP1 [86] to promote HR [87]. If the relative pools of REV7 in complex with its various partners vary between different cell types, this could well explain how TRIP13-mediated dissociation of REV7 protein complexes has pleiotropic effects on HR in different cells.

It is also possible that the effects of TRIP13 on DDR are mediated by REV7-independent mechanisms. Some studies have found that TRIP13 promotes NHEJ directly [76, 77]. For example, TRIP13 interacts with DNA-PKcs complex proteins to stimulate NHEJ, even in HR-sufficient cells [76]. TRIP13 also facilitates the interaction between MDC1 and the MRN complex to promote and amplify ATM signaling [77]. The REV7-related germ cell protein HORMAD1 is also a probable TRIP13 target, since it is removed from the synaptonemal complex of unsynapsed meiotic chromosomes in a TRIP13-dependent manner [88]. HORMAD1 is a cancer/testis antigen that is misexpressed in many cancer cells where it promotes HR [89, 90]. Although the putative binding partner of HORMAD1 in promoting HR in cancer cells is unknown, it is likely that HR-stimulatory HORMAD1 protein complexes would also be dissociated by TRIP13. Since HORMAD1 expression in cancer cells is highly variable, TRIP13 could have very different effects on HR in different cancer cells depending on their HORMAD1 status. Similarly, variability in the availability or deployment of any TRIP13-interacting DDR factors and pathways might determine how TRIP13 inhibition affects DNA repair in different cancer cells.

While this work was in progress, two other studies demonstrated enrichment of TRIP13 expression in PDAC and other gastrointestinal tumors when compared with normal tissues [83, 91]. Consistent with our study, Afaq *et al.* also showed that TRIP13 depletion led to reduced growth of PDAC cell lines cultured *in vitro* and when xenografted into mice [91]. Moreover, Afaq *et al.* demonstrated that genetic or pharmacological ablation of TRIP13 led to increased gemcitabine sensitivity in cultured cells and *in vivo* [91]. Mechanistically, those workers suggested that TRIP13 sustains tumorigenic characteristics in PDAC by maintaining expression of FGFR4, phosphorylation of STAT1, and WNT/β-catenin signaling [91]. It will be interesting to determine whether TRIP13 sustains tumorigenic signaling pathways (such as FGFR4, STAT1, and WNT/β-catenin) secondarily to its role in tolerating DNA replication stress, or instead whether protein complexes targeted by TRIP13 modulate mitogenic signaling directly independently of the DDR. Owing to its upregulated expression in cancer cells and its roles in sustaining neoplastic cells and pharmacological tractability, TRIP13 remains a very attractive therapeutic target [92].

Since TRIP13 has pleiotropic roles in the DDR and other processes, it is necessary to determine how the various TRIP13 effector pathways function in cancer cells. Elucidating how TRIP13-interacting pathways are wired in different cancer settings may reveal opportunities for precision medicine, e.g. by identifying those tumors that are most sensitive to TRIP13 inhibitors alone or in combination with other agents (such as PARP or TLS inhibitors).

Acknowledgements

We thank Dr Pablo Ariel for his assistance in microscopy image acquisition. Microscopy was performed at the Microscopy Services Laboratory at the University of North Carolina at Chapel Hill, which is supported in part by P30 CA016086 Cancer Center Core Support Grant to the UNC Lineberger Comprehensive Cancer Center. The Andor Dragonfly microscope was funded with support from National Institutes of Health grant S10OD030223.

Author contributions: Conceptualization, Project Administration, Resources, Software, Writing-Original Draft by J.R.A. and C.V.; Data Curation by J.R.A. and G.N.D., Formal Analysis and Visualization by J.R.A., G.N.D. and U.P.; Funding Acquisition by C.V.; Investigation by J.R.A., G.N.D., S.J., U.P., X.Z., and J.A.K.; Methodology by J.R.A, C.J.D., J.E.P., S.C.W., J.L.B., and C.V.; Supervision by C.J.D., J.E.P., S.C.W., J.L.B., and C.V.; Writing - Review & Editing by J.R.A., G.N.D., S.J., U.P., X.Z., J.A.K., C.J.D., J.E.P., S.C.W., J.L.B., and C.V.

Supplementary data

Supplementary data is available at NAR Cancer online.

Conflict of interest

None declared.

Funding

This work was supported by grants (R01 ES009558, CA215347, CA229530) from the National Institutes of Health to C.V. Research reported in this publication was supported in part by the North Carolina Biotechnology Center Institutional Support Grant 2012-IDG-1006. *In vivo* experiments were performed by the UNC Lineberger Preclinical Research Unit (PRU) at the University of North Carolina at Chapel Hill, which is supported in part by an National Cancer Institute (NCI) Center Core Support Grant (CA16086) to the UNC Lineberger Comprehensive Cancer Center.

Data availability

RNA-seq data for hTERT-HPNE cells underlying this article are available in BioProject ID PRJNA1137433. The TCGA pancreatic adenocarcinoma (TCGA-PAAD) data were retrieved using TCGAbiolinks R package (version 2.30.0) and are available on TCGA portal (https://portal.gdc.cancer.gov/). Unnormalized counts and differential gene expression statistics are available in Supplementary Table S2. Steps, criteria, and code used for HPNE differential gene expression analysis, TCGA-PAAD analysis, and PHATE analysis using 4i experiments are available at https://github.com/vazirilb/PancreaticCancer-DifferentialExpression-4iPHATE and https://zenodo.org/records/14982910.

References

1. Svegliati S, Cancello R, Sambo P *et al.* Platelet-derived growth factor and reactive oxygen species (ROS) regulate Ras protein levels in primary human fibroblasts via ERK1/2. Amplification of ROS and Ras in systemic sclerosis fibroblasts. *J Biol Chem* 2005;**280**:36474–82. https://doi.org/10.1074/jbc.M502851200
2. Nitta M, Kozono D, Kennedy R *et al.* Targeting EGFR induced oxidative stress by PARP1 inhibition in glioblastoma therapy. *PLoS One* 2010;**5**:e10767. https://doi.org/10.1371/journal.pone.0010767
3. Westermark UK, Lindberg N, Roswall P *et al.* RAD51 can inhibit PDGF-B-induced gliomagenesis and genomic instability. *Neuro Oncol* 2011;**13**:1277–87. https://doi.org/10.1093/neuonc/nor131
4. Lindberg N, Holland EC. PDGF in gliomas: more than just a growth factor? *Ups J Med Sci* 2012;**117**:92–8. https://doi.org/10.3109/03009734.2012.654860
5. Cheng Y, Li W, Gui R *et al.* Dual characters of GH-IGF1 signaling pathways in radiotherapy and post-radiotherapy repair of cancers. *Front Cell Dev Biol* 2021;**9**:671247. https://doi.org/10.3389/fcell.2021.671247
6. Chesnokova V, Zonis S, Barrett RJ *et al.* Growth hormone induces colon DNA damage independent of IGF-1. *Endocrinology* 2019;**160**:1439–47. https://doi.org/10.1210/en.2019-00132
7. Vafa O, Wade M, Kern S *et al.* c-Myc can induce DNA damage, increase reactive oxygen species, and mitigate p53 function: a mechanism for oncogene-induced genetic instability. *Mol Cell* 2002;**9**:1031–44. https://doi.org/10.1016/S1097-2765(02)00520-8
8. Harrington EA, Bennett MR, Fanidi A *et al.* c-Myc-induced apoptosis in fibroblasts is inhibited by specific cytokines. *EMBO J* 1994;**13**:3286–95. https://doi.org/10.1002/j.1460-2075.1994.tb06630.x
9. Evan GI, Wyllie AH, Gilbert CS *et al.* Induction of apoptosis in fibroblasts by c-myc protein. *Cell* 1992;**69**:119–28. https://doi.org/10.1016/0092-8674(92)90123-T
10. Zindy F, Eischen CM, Randle DH *et al.* Myc signaling via the ARF tumor suppressor regulates p53-dependent apoptosis and immortalization. *Genes Dev* 1998;**12**:2424–33. https://doi.org/10.1101/gad.12.15.2424
11. Macheret M, Halazonetis TD. Intragenic origins due to short G1 phases underlie oncogene-induced DNA replication stress. *Nature* 2018;**555**:112–6. https://doi.org/10.1038/nature25507
12. Srinivasan SV, Dominguez-Sola D, Wang LC *et al.* Cdc45 is a critical effector of myc-dependent DNA replication stress. *Cell Rep* 2013;**3**:1629–39. https://doi.org/10.1016/j.celrep.2013.04.002
13. Ray S, Atkuri KR, Deb-Basu D *et al.* MYC can induce DNA breaks *in vivo* and *in vitro* independent of reactive oxygen species. *Cancer Res* 2006;**66**:6598–605. https://doi.org/10.1158/0008-5472.CAN-05-3115
14. Bartkova J, Rezaei N, Liontos M *et al.* Oncogene-induced senescence is part of the tumorigenesis barrier imposed by DNA damage checkpoints. *Nature* 2006;**444**:633–7. https://doi.org/10.1038/nature05268
15. Costantino L, Sotiriou SK, Rantala JK *et al.* Break-induced replication repair of damaged forks induces genomic duplications in human cells. *Science* 2014;**343**:88–91. https://doi.org/10.1126/science.1243211
16. Minella AC, Swanger J, Bryant E *et al.* p53 and p21 form an inducible barrier that protects cells against cyclin E-cdk2 deregulation. *Curr Biol* 2002;**12**:1817–27. https://doi.org/10.1016/S0960-9822(02)01225-3
17. Jones RM, Mortusewicz O, Afzal I *et al.* Increased replication initiation and conflicts with transcription underlie Cyclin E-induced replication stress. *Oncogene* 2013;**32**:3744–53. https://doi.org/10.1038/onc.2012.387
18. Xu M, Yu Q, Subrahmanyam R *et al.* Beta-catenin expression results in p53-independent DNA damage and oncogene-induced senescence in prelymphomagenic thymocytes *in vivo*. *Mol Cell Biol* 2008;**28**:1713–23. https://doi.org/10.1128/MCB.01360-07
19. Rai P, Young JJ, Burton DG *et al.* Enhanced elimination of oxidized guanine nucleotides inhibits oncogenic RAS-induced DNA damage and premature senescence. *Oncogene* 2011;**30**:1489–96. https://doi.org/10.1038/onc.2010.520
20. Maya-Mendoza A, Ostrakova J, Kosar M *et al.* Myc and Ras oncogenes engage different energy metabolism programs and evoke distinct patterns of oxidative and DNA replication stress. *Mol Oncol* 2015;**9**:601–16. https://doi.org/10.1016/j.molonc.2014.11.001
21. Di Micco R, Sulli G, Dobreva M *et al.* Interplay between oncogene-induced DNA damage response and heterochromatin in senescence and cancer. *Nat Cell Biol* 2011;**13**:292–302. https://doi.org/10.1038/ncb2170
22. Hills SA, Diffley JF. DNA replication and oncogene-induced replicative stress. *Curr Biol* 2014;**24**:R435–44. https://doi.org/10.1016/j.cub.2014.04.012
23. Bowry A, Kelly RDW, Petermann E. Hypertranscription and replication stress in cancer. *Trends Cancer* 2021;**7**:863–77. https://doi.org/10.1016/j.trecan.2021.04.006
24. Kotsantis P, Petermann E, Boulton SJ. Mechanisms of oncogene-induced replication stress: jigsaw falling into place. *Cancer Discov* 2018;**8**:537–55. https://doi.org/10.1158/2159-8290.CD-17-1461
25. Peripolli S, Meneguello L, Perrod C *et al.* Oncogenic c-Myc induces replication stress by increasing cohesins chromatin occupancy in a CTCF-dependent manner. *Nat Commun* 2024;**15**:1579. https://doi.org/10.1038/s41467-024-45955-z
26. Yang Y, Gao Y, Mutter-Rottmayer L *et al.* DNA repair factor RAD18 and DNA polymerase Polκ confer tolerance of oncogenic DNA replication stress. *J Cell Biol* 2017;**216**:3097–115. https://doi.org/10.1083/jcb.201702006
27. Dagg RA, Zonderland G, Lombardi EP *et al.* A transcription-based mechanism for oncogenic beta-catenin-induced lethality in BRCA1/2-deficient cells. *Nat Commun* 2021;**12**:4919. https://doi.org/10.1038/s41467-021-25215-0
28. Neelsen KJ, Zanini IM, Herrador R *et al.* Oncogenes induce genotoxic stress by mitotic processing of unusual replication intermediates. *J Cell Biol* 2013;**200**:699–708. https://doi.org/10.1083/jcb.201212058
29. Zeng J, Hills SA, Ozono E *et al.* Cyclin E-induced replicative stress drives p53-dependent whole-genome duplication. *Cell* 2023;**186**:528–42. https://doi.org/10.1016/j.cell.2022.12.036
30. Gallo D, Young JTF, Fourtounis J *et al.* CCNE1 amplification is synthetic lethal with PKMYT1 kinase inhibition. *Nature* 2022;**604**:749–56. https://doi.org/10.1038/s41586-022-04638-9
31. Mayers JR, Torrence ME, Danai LV *et al.* Tissue of origin dictates branched-chain amino acid metabolism in mutant Kras-driven cancers. *Science* 2016;**353**:1161–5. https://doi.org/10.1126/science.aaf5171
32. Cook JH, Melloni GEM, Gulhan DC *et al.* The origins and genetic interactions of KRAS mutations are allele- and tissue-specific. *Nat*

Commun 2021;**12**:1808. https://doi.org/10.1038/s41467-021-22125-z

33. Le Roux O, Pershing NLK, Kaltenbrun E *et al.* Genetically manipulating endogenous Kras levels and oncogenic mutations *in vivo* influences tissue patterning of murine tumorigenesis. *eLife* 2022;**11**:e75715. https://doi.org/10.7554/eLife.75715
34. Guerra C, Mijimolle N, Dhawahir A *et al.* Tumor induction by an endogenous K-ras oncogene is highly dependent on cellular context. *Cancer Cell* 2003;**4**:111–20. https://doi.org/10.1016/S1535-6108(03)00191-0
35. Vaziri C, Rogozin IB, Gu Q *et al.* Unravelling roles of error-prone DNA polymerases in shaping cancer genomes. *Oncogene* 2021;**40**:6549–65. https://doi.org/10.1038/s41388-021-02032-9
36. Schoppy DW, Ragland RL, Gilad O *et al.* Oncogenic stress sensitizes murine cancers to hypomorphic suppression of ATR. *J Clin Invest* 2012;**122**:241–52. https://doi.org/10.1172/JCI58928
37. Efeyan A, Murga M, Martinez-Pastor B *et al.* Limited role of murine ATM in oncogene-induced senescence and p53-dependent tumor suppression. *PLoS One* 2009;**4**:e5475. https://doi.org/10.1371/journal.pone.0005475
38. Hingorani SR, Tuveson DA. Ras redux: rethinking how and where Ras acts. *Curr Opin Genet Dev* 2003;**13**:6–13.
39. Haigis KM, Cichowski K, Elledge SJ. Tissue-specificity in cancer: the rule, not the exception. *Science* 2019;**363**:1150–1. https://doi.org/10.1126/science.aaw3472
40. Poulin EJ, Bera AK, Lu J *et al.* Tissue-specific oncogenic activity of KRAS^{A146T}. *Cancer Discov* 2019;**9**:738–55. https://doi.org/10.1158/2159-8290.CD-18-1220
41. Brubaker DK, Paulo JA, Sheth S *et al.* Proteogenomic network analysis of context-specific KRAS signaling in mouse-to-human cross-species translation. *Cell Syst* 2019;**9**:258–70. https://doi.org/10.1016/j.cels.2019.07.006
42. Halfon MS, Carmena A, Gisselbrecht S *et al.* Ras pathway specificity is determined by the integration of multiple signal-activated and tissue-restricted transcription factors. *Cell* 2000;**103**:63–74. https://doi.org/10.1016/S0092-8674(00)00105-7
43. Waters AM, Der CJ. KRAS: the critical driver and therapeutic target for pancreatic cancer. *Cold Spring Harb Perspect Med* 2018;**8**:a031435. https://doi.org/10.1101/cshperspect.a031435
44. Bryant KL, Mancias JD, Kimmelman AC *et al.* KRAS: feeding pancreatic cancer proliferation. *Trends Biochem Sci* 2014;**39**:91–100. https://doi.org/10.1016/j.tibs.2013.12.004
45. Kleeff J, Korc M, Apte M *et al.* Pancreatic cancer. *Nat Rev Dis Primers* 2016;**2**:16022. https://doi.org/10.1038/nrdp.2016.22
46. Rawla P, Sunkara T, Gaduputi V. Epidemiology of pancreatic cancer: global trends, etiology and risk factors. *World J Oncol* 2019;**10**:10–27. https://doi.org/10.14740/wjon1166
47. Siegel RL, Miller KD, Jemal A. Cancer statistics, 2018. *CA Cancer J Clin* 2018;**68**:7–30. https://doi.org/10.3322/caac.21442
48. Siegel RL, Giaquinto AN, Jemal A. Cancer statistics, 2024. *CA Cancer J Clin* 2024;**74**:12–49. https://doi.org/10.3322/caac.21820
49. Bekaii-Saab TS, YR S.A., Buchschacher GL *et al.* KRYSTAL-1: updated activity and safety of adagrasib (MRTX849) in patients (Pts) with unresectable or metastatic pancreatic cancer (PDAC) and other gastrointestinal (GI) tumors harboring a KRAS^{G12C} mutation. *J Clin Oncol* 2022;**40**:519. https://doi.org/10.1200/JCO.2022.40.4_suppl.519
50. Strickler JH, HA S.H., Sunakawa Y *et al.* First data for sotorasib in patients with pancreatic cancer with KRAS p.G12C mutation: a phase I/II study evaluating efficacy and safety.. *J Clin Oncol* 2022;**40**:360490. https://doi.org/10.1200/JCO.2022.40.36_suppl.360490
51. Muzumdar MD, Chen PY, Dorans KJ *et al.* Survival of pancreatic cancer cells lacking KRAS function. *Nat Commun* 2017;**8**:1090. https://doi.org/10.1038/s41467-017-00942-5
52. Chen PY, Muzumdar MD, Dorans KJ *et al.* Adaptive and reversible resistance to Kras inhibition in pancreatic cancer cells. *Cancer Res* 2018;**78**:985–1002. https://doi.org/10.1158/0008-5472.CAN-17-2129
53. Nollmann FI, Ruess DA. Targeting mutant KRAS in pancreatic cancer: futile or promising? *Biomedicines* 2020;**8**:281. https://doi.org/10.3390/biomedicines8080281
54. Awad MM, Liu S, Rybkin II *et al.* Acquired resistance to KRAS^{G12C} inhibition in cancer. *N Engl J Med* 2021;**384**:2382–93. https://doi.org/10.1056/NEJMoa2105281
55. Kemp SB, Cheng N, Markosyan N *et al.* Efficacy of a small-molecule inhibitor of Kras^{G12D} in immunocompetent models of pancreatic cancer. *Cancer Discov* 2023;**13**:298–311. https://doi.org/10.1158/2159-8290.CD-22-1066
56. Hallin J, Bowcut V, Calinisan A *et al.* Anti-tumor efficacy of a potent and selective non-covalent KRAS^{G12D} inhibitor. *Nat Med* 2022;**28**:2171–82. https://doi.org/10.1038/s41591-022-02007-7
57. Wang Z, Li Y, Ahmad A *et al.* Pancreatic cancer: understanding and overcoming chemoresistance. *Nat Rev Gastroenterol Hepatol* 2011;**8**:27–33. https://doi.org/10.1038/nrgastro.2010.188
58. Beutel AK, Halbrook CJ. Barriers and opportunities for gemcitabine in pancreatic cancer therapy. *Am J Physiol Cell Physiol* 2023;**324**:C540–52.
59. Stathis A, Moore MJ. Advanced pancreatic carcinoma: current treatment and future challenges. *Nat Rev Clin Oncol* 2010;**7**:163–72. https://doi.org/10.1038/nrclinonc.2009.236
60. Perkhofer L, Gout J, Roger E *et al.* DNA damage repair as a target in pancreatic cancer: state-of-the-art and future perspectives. *Gut* 2021;**70**:606–17. https://doi.org/10.1136/gutjnl-2019-319984
61. Lee KM, Yasuda H, Hollingsworth MA *et al.* Notch 2-positive progenitors with the intrinsic ability to give rise to pancreatic ductal cells. *Lab Invest* 2005;**85**:1003–12. https://doi.org/10.1038/labinvest.3700298
62. Hill W, Zaragkoulias A, Salvador-Barbero B *et al.* EPHA2-dependent outcompetition of KRAS^{G12D} mutant cells by wild-type neighbors in the adult pancreas. *Curr Biol* 2021;**31**:2550–60. https://doi.org/10.1016/j.cub.2021.03.094
63. Iacobuzio-Donahue CA. Genetic evolution of pancreatic cancer: lessons learnt from the pancreatic cancer genome sequencing project. *Gut* 2012;**61**:1085–94. https://doi.org/10.1136/gut.2010.236026
64. Fiordalisi JJ, Johnson RL 2nd, Ulku AS *et al.* Mammalian expression vectors for Ras family proteins: generation and use of expression constructs to analyze Ras family function. *Methods Enzymol* 2001;**332**:3–36. https://doi.org/10.1016/S0076-6879(01)32189-4
65. Zhang X, Joseph S, Wu D *et al.* The DNA damage response (DDR) landscape of endometrial cancer defines discrete disease subtypes and reveals therapeutic opportunities. *NAR Cancer* 2024;**6**:zcae015. https://doi.org/10.1093/narcan/zcae015
66. Wang Y, Risteski P, Yang Y *et al.* The TRIM69–MST2 signaling axis regulates centrosome dynamics and chromosome segregation. *Nucleic Acids Res* 2023;**51**:10568–89. https://doi.org/10.1093/nar/gkad766
67. Cheng X, An J, Lou J *et al.* Trans-lesion synthesis and mismatch repair pathway crosstalk defines chemoresistance and hypermutation mechanisms in glioblastoma. *Nat Commun* 2024;**15**:10568–89. https://doi.org/10.1038/s41467-024-45979-5
68. Matson JP, Dumitru R, Coryell P *et al.* Rapid DNA replication origin licensing protects stem cell pluripotency. *eLife* 2017;**6**:e30473. https://doi.org/10.7554/eLife.30473
69. Cancer Genome Atlas Research Network. Integrated genomic characterization of pancreatic ductal adenocarcinoma. *Cancer Cell* 2017;**32**:185–203. https://doi.org/10.1016/j.ccell.2017.07.007
70. Stallaert W, Kedziora KM, Taylor CD *et al.* The structure of the human cell cycle. *Cell Syst* 2022;**13**:230–40. https://doi.org/10.1016/j.cels.2021.10.007
71. Moon KR, van Dijk D, Wang Z *et al.* Visualizing structure and transitions in high-dimensional biological data. *Nat Biotechnol* 2019;**37**:1482–92. https://doi.org/10.1038/s41587-019-0336-3

72. Ceccaldi R, Liu JC, Amunugama R *et al.* Homologous-recombination-deficient tumours are dependent on Polθ-mediated repair. *Nature* 2015;**518**:258–62. https://doi.org/10.1038/nature14184
73. Klomp JA, Klomp JE, Stalnecker CA *et al.* Defining the KRAS- and ERK-dependent transcriptome in KRAS-mutant cancers. *Science* 2024;**384**:eadk0775. https://doi.org/10.1126/science.adk0775
74. Clairmont CS, D'Andrea AD. REV7 directs DNA repair pathway choice. *Trends Cell Biol* 2021;**31**:965–78. https://doi.org/10.1016/j.tcb.2021.05.009
75. Helleday T. The underlying mechanism for the PARP and BRCA synthetic lethality: clearing up the misunderstandings. *Mol Oncol* 2011;**5**:387–93. https://doi.org/10.1016/j.molonc.2011.07.001
76. Banerjee R, Russo N, Liu M *et al.* TRIP13 promotes error-prone nonhomologous end joining and induces chemoresistance in head and neck cancer. *Nat Commun* 2014;**5**:4527. https://doi.org/10.1038/ncomms5527
77. Jeong H, Wie M, Baek IJ *et al.* TRIP13 participates in immediate-early sensing of DNA strand breaks and ATM signaling amplification through MRE11. *Cells* 2022;**11**:4095. https://doi.org/10.3390/cells11244095
78. Wojtaszek JL, Chatterjee N, Najeeb J *et al.* A small molecule targeting mutagenic translesion synthesis improves chemotherapy. *Cell* 2019;**178**:152–9. https://doi.org/10.1016/j.cell.2019.05.028
79. Joseph S, Zhang X, Droby GN *et al.* MAPK14/p38alpha shapes the molecular landscape of endometrial cancer and promotes tumorigenic characteristics. *Cell Rep* 2025;**44**:115104. https://doi.org/10.1016/j.celrep.2024.115104
80. Cong K, Cantor SB. Exploiting replication gaps for cancer therapy. *Mol Cell* 2022;**82**:2363–9. https://doi.org/10.1016/j.molcel.2022.04.023
81. Cong K, Peng M, Kousholt AN *et al.* Replication gaps are a key determinant of PARP inhibitor synthetic lethality with BRCA deficiency. *Mol Cell* 2021;**81**:3227. https://doi.org/10.1016/j.molcel.2021.07.015
82. Etemadmoghadam D, Weir BA, Au-Yeung G *et al.* Synthetic lethality between CCNE1 amplification and loss of BRCA1. *Proc Natl Acad Sci USA* 2013;**110**:19489–94. https://doi.org/10.1073/pnas.1314302110
83. Dhasmana S, Dhasmana A, Rios S *et al.* An integrated computational biology approach defines the crucial role of TRIP13 in pancreatic cancer. *Comput Struct Biotechnol J* 2023;**21**:5765–75. https://doi.org/10.1016/j.csbj.2023.11.029
84. Clairmont CS, Sarangi P, Ponnienselvan K *et al.* TRIP13 regulates DNA repair pathway choice through REV7 conformational change. *Nat Cell Biol* 2020;**22**:87–96. https://doi.org/10.1038/s41556-019-0442-y
85. de Krijger I, Fohr B, Perez SH *et al.* MAD2L2 dimerization and TRIP13 control shieldin activity in DNA repair. *Nat Commun* 2021;**12**:5421. https://doi.org/10.1038/s41467-021-25724-y
86. Hara K, Taharazako S, Ikeda M *et al.* Dynamic feature of mitotic arrest deficient 2-like protein 2 (MAD2L2) and structural basis for its interaction with chromosome alignment-maintaining phosphoprotein (CAMP). *J Biol Chem* 2017;**292**:17658–67. https://doi.org/10.1074/jbc.M117.804237
87. Li F, Sarangi P, Iyer DR *et al.* CHAMP1 binds to REV7/FANCV and promotes homologous recombination repair. *Cell Rep* 2022;**40**:111297. https://doi.org/10.1016/j.celrep.2022.111297
88. Chotiner JY, Leu NA, Yang F *et al.* TRIP13 localizes to synapsed chromosomes and functions as a dosage-sensitive regulator of meiosis. *eLife* 2024;**12**:RP92195. https://doi.org/10.7554/eLife.92195
89. Gao Y, Kardos J, Yang Y *et al.* The cancer/testes (CT) antigen HORMAD1 promotes homologous recombinational DNA repair and radioresistance in lung adenocarcinoma cells. *Sci Rep* 2018;**8**:15304. https://doi.org/10.1038/s41598-018-33601-w
90. Nichols BA, Oswald NW, McMillan EA *et al.* HORMAD1 is a negative prognostic indicator in lung adenocarcinoma and specifies resistance to oxidative and genotoxic stress. *Cancer Res* 2018;**78**:6196–208. https://doi.org/10.1158/0008-5472.CAN-18-1377
91. Afaq F, Agarwal S, Bajpai P *et al.* Targeting of oncogenic AAA-ATPase TRIP13 reduces progression of pancreatic ductal adenocarcinoma. *Neoplasia* 2024;**47**:100951. https://doi.org/10.1016/j.neo.2023.100951
92. Lu S, Qian J, Guo M *et al.* Insights into a crucial role of TRIP13 in human cancer. *Comput Struct Biotechnol J* 2019;**17**:854–61. https://doi.org/10.1016/j.csbj.2019.06.005

Received: July 24, 2024. **Revised:** January 25, 2025. **Editorial Decision:** March 5, 2025. **Accepted:** March 11, 2025